THE EFFECTOF RESIDUAL STRESS ON STRESS CORROSION CRACKING IN MARAGING STEEL BLADES

A Thesis

Presented to

The Faculty of the Department of Physics

California State University, Los Angeles

In Partial Fulfillment

of the Requirements for the Degree

Master of Science

in

Physics

By

Alexander Kass

May 2018

LIGO DOC P1800124

The thesis of Alexander Jonathan Kass is approved.

Riccardo DeSalvo, Committee Chair

Jose Rodriguez

Guo-Meng Zhao

Radi Jishi, Department Chair

California State University, Los Angeles

May 2018

ABSTRACT

Effect of Residual Stress on Stress Corrosion Cracking in Maraging Steel Blades

By

Alexander Kass

Maraging Steel blades are employed for the attenuation of Earth's vibrational motion in the VIRGO and LIGO interferometers. In VIRGO many units failed catastrophically after exposure to environmental air. Stress corrosion cracking is determined upon inspection. Notably, the failed units were ground to final thickness, which removed a layer likely under compression stress, and/or were resolubilized which has a similar effect. Blades that were made of untreated, cold rolled sheets are largely immune from this failure, despite coming from the same source. This thesis will attempt to confirm using X-Ray Diffraction and theory that the residual stress from cold rolling retards the progress of crack formation and propagation and that Stress Corrosion Cracking was inhibited in some blades by the layer of residual stress left by the cold rolling process. This knowledge will allow production of safer blades in the future. Diffraction measurements yielded confirmation that a compressive layer exists on the surface of the cold rolled blades, with a stress value of approximately -300MPa. This result was confirmed by comparing samples to maraging steel blades first ground to eliminate the surface layer, then manually cold rolled and finally precipitation hardened.

ACKNOWLEDGMENTS

I want to express my sincerest gratitude towards all the faculty members and peers from CSULA I worked with. My teachers and peers here, comprise some of the best people I know, and they've been vital in my growth and advancement. Professors DeSalvo, Rodriguez, and Zhao all made this thesis possible and I am indebted to them for sharing their wisdom with me.

Some enormous thanks go to Katherine Nelms, who volunteered her time to helping this research progress. Thanks to Professor Yang, who generously shared her laboratory with us and made the whole endeavor possible. Thanks to Matt Gonzales for carrying on with the work.

Thanks to the LIGO/VIRGO project for their generous assistance with NSF-CCR Grant NSF/PHY-1707868/2-31491. This is Publication: LIGO-P1800124.

TABLE OF CONTENTS

LIST OF TABLES

Table

LIST OF FIGURES

Figure

LIST OF TERMS

AD	Aubert Duval, steel manufacturer
GM	Galli & Morelli, metal grinding servicer
CR	Cold Rolled
LR	Lab (Cold) Rolled
XRD	X-Ray Diffraction
FCC	Face Centered Cubic
BCC	Body Centered Cubic
BCT	Body Centered Tetragonal

CHAPTER 1

Introduction

Maraging Steel blades are currently being employed in all gravitational wave detectors; an example is shown in figure 1 [1].

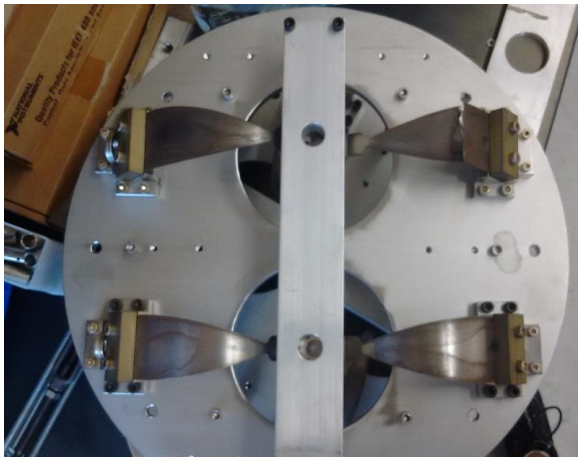

Figure 1. Crack turns into a complete fracture in a Maraging Steel Blade which has penetrated through the thickness of the steel. SCC is suspected.

They operate as cantilever beams, circularly arranged into a filter, under a bending moment, supporting a heavily weighted wire. Unfortunately, in VIRGO several of the blades within these filters catastrophically failed during maintenance, cracking through the thickness of the blade; this cost the collaboration precious operation time and money. The exact cause of failure was not immediately apparent, but a close inspection suggested Stress Corrosion Cracking (SCC) [2]. Researchers involved with this project noticed:

- The breakages occurred within weeks after the inside of the superattenuator tower was accidentally exposed to environmental humidity.

- The blades were not all identical; those that broke were typically either resolubilized or of a ground-to-thickness type. All blades were made with material supplied by Aubert Duval.
- The cracks were almost entirely mode 1 type and intergranular.

Scientists in all Gravitational Wave Detectors need to make certain that such accidents cannot happen in the future; thus, new blades which possess greater durability against SCC, or a strategy to avoid SCC failure are necessary. A likely explanation is that the maraging steel blades that were cold rolled did not break because of a mechanical or chemical difference they possessed from the ground-to-thickness units; residual stress is a reasonable explanation. This rationalization suggests that cold-rolling-induced plastic deformation, which results in a net, static compressional stress on the outer faces of sheet metal, may cause the better durability of some blades [3].

This residual surface compression will have the effect of neutralizing tensile stress experienced when loaded, that would otherwise cause SCC [3]. Particularly due to the manner that these blades are operated (bending), the residual stress will superpose on the regions of highest tensional stress during bending operation, on the upper surface. In this region, mode 1 cracking initiates and in the case high strength steel, quickly propagates to catastrophic failure [3]. This author asserts that residual compressional stress in maraging steel blades may be the agent that inhibits stress corrosion cracking. A variety of methods were employed to prove that the cold rolled blades did possess a residual stress while the ground-to-thickness units did not. If proven true, this will further suggest the possibility that residual stress from cold rolling inhibits SCC in Maraging Steel.

1.1 Virgo Gravitational Wave Observatory

To put the blade failure into context, consider the apparatus that employs it. Dozens of such maraging steel blades are instrumental in supporting the optomechanical assembly inside of the Laser Interferometer Gravitational-Wave Observatory, VIRGO, as elements in seismic attenuation [1]. The most catastrophic failures happened in VIRGO [2].

Figure 2. VIRGO. Pisa, Italy. [47]

VIRGO is a massive Michaelson interferometer located in Pisa, Italy, which measures contractions in space caused by the propagation of gravitational waves. Along with two other similar interferometers in the US, detections of no less than 6 astronomical merging events, 5 black hole pairs, and 1 neutron star pair have been made [4].

The physical wave passing through earth is extremely small, with wavelengths on the order $\Delta L = 10^{-9} nm$, roughly $\frac{1}{1{,}000}$ the size of a proton [5] in a km sized detector.

To detect these tiny gravitational waves, however, the Michaelson must satisfy strict design requirements. The light passing between the two paths recombine and

produce an interference pattern on the light detector which depends on the phase difference $\Delta\phi$ between the arms. The phase difference $\Delta\phi$ can then be used to determine ΔL generated by a gravitational wave.

$$\Delta\phi = \frac{2\pi}{\lambda}\Delta L$$

The actual measurement of these interference patterns is done with digital electronics that measure intensity and perform post processing as well. Sensitivity of such a system must be extremely small to allow for measurements of tiny ΔL. Letting *h* be the sensitivity, it is approximated by [6]:

$$h \sim \frac{\Delta L}{L}$$

and enforces the requirement that L, the interferometer optical path length, be very long.

While noise is omnipresent in the system from a variety of sources, physical vibrations of the earth due to seismic activity are quite dangerous and of interest in this case; their net effect on operation is a reduction in range for detection [1]. For this reason, a sophisticated and large isolation system is necessary to keep vibration amplitudes of all optomechanical components, such as the mirrors, smaller than ΔL, 10^{-9} nm [1]. Ultimately the solution decided upon was to isolate the mirror by suspending it from a steel wire and cantilever blades in what is aptly called a “superattenuator”; the Virgo design’s rough drawing is shown in figure 3 [1].

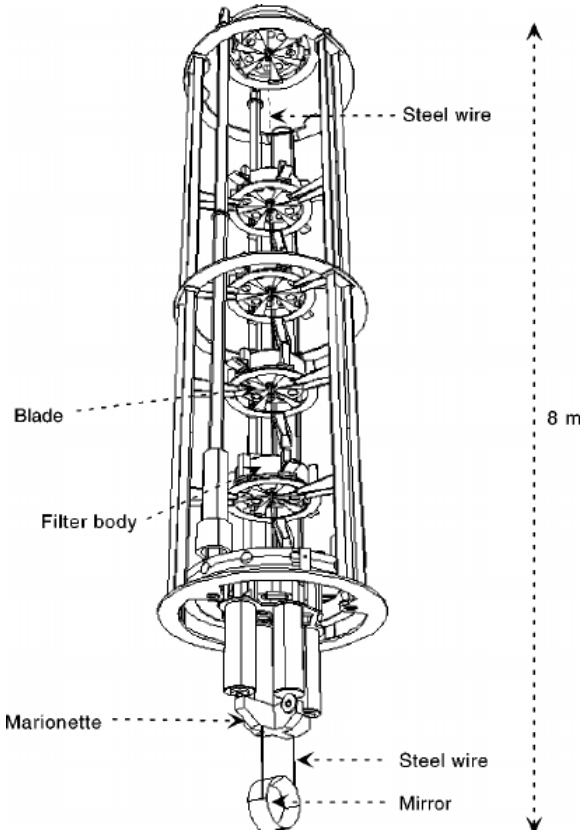

Figure 3. Drawing of the VIRGO superattenuator tower

The required attenuation would arise from a chain of several filters, like the setup in figure 3, attached to the structure on the outside. Each filter is made of several maraging steel blades in a circle, attached to a wire suspending another. The blades are bent down in cantilever fashion; these units support the weight of the mirror test mass.

1.2 Maraging Steel

Maraging Steel is a carbon-free, high strength iron alloy very well suited to tough tasks and heavy loads, such as in airplane landing gears and weaponry. Therefore, it is also a very reasonable choice for the high stress in seismic attenuation systems. The name derives from a mixture of "Martensite", an iron crystal lattice (α'-Fe), and "Aging" also known as precipitation hardening [7].

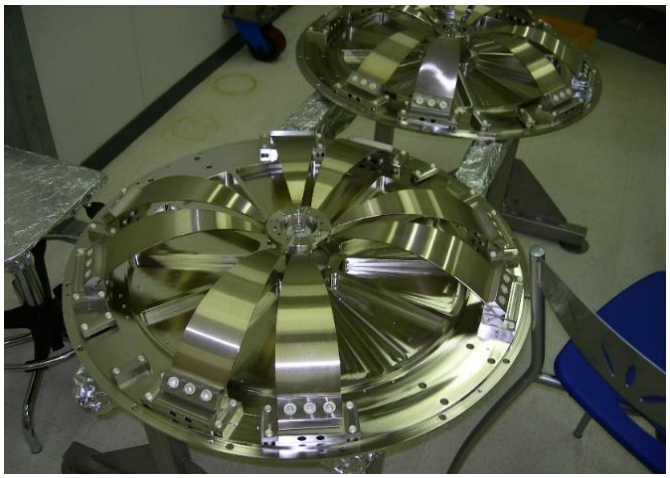

Figure 4. A prototype filter made up of 8 maraging steel blades.

Maraging is manufactured by a series of steps to first produce a Martensite alloy lattice (α'-Fe) during cooling; before being aged at a certain temperature (400-500˚C), typically [7]. The process is of course not so simple; after the initial melt, cooling is done rapidly to force the initially occurring Austenite (γ-Fe) Face Centered Cubic (FCC) lattice to undergo a phase change into a Body Centered Tetragonal (BCT) martensite. As will be discussed later, this Tetragonal geometry is very similar to BCC (α-Fe) ferrite and in this case can be assumed as equal, because carbon % is very low [7].

The liquid metal will have nucleation points during cooling, from where separate, uncoordinated lattices will grow. A single crystal metal is unattainable in relevant sizes and quantities, and instead many separate crystals grow into each other wherein the entire piece becomes solid. These separate crystals, or "grains," are not oriented along a common reference frame but together compose a polycrystalline solid [7].

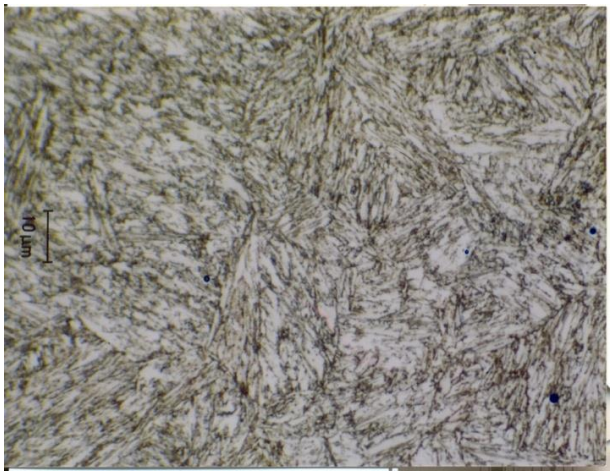

Figure 5. Maraging Steel at high magnification [8]

1.2.1 Precipitation Hardening

The properties of maraging steel arise from its martensite lattice, as well as the alloying elements it contains and their response to aging. When the metal is heated to temperatures of ~ 400-500˚C, the nickel and other alloy components can precipitate within the iron lattice forming billions of nanometric scale structures peppering each grain, in sizes of tens of microns or less [9].

The recipe for the Marval18 Maraging Steel used in Virgo are shows in table 1 [10]. This is a relatively common makeup for maraging steel and provides an approximate reference point for comparing to other maraging steels in literature. This alloy is approximately analogous to (18Ni) Maraging 250 [11].

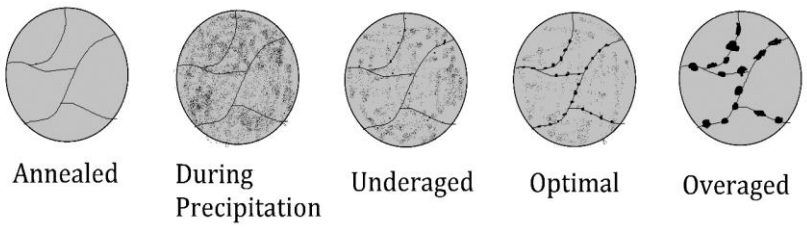

Figure 6. General mechanism of aging, to no scale.

Table 1

Chemical Composition of Marval18 Maraging Steel as Prescribed by the Aubert Duval Specification Sheet. Key Points are that Maraging is a Carbon-free Alloy, that Nickel, Cobalt, and Molybdenum are the Metals that will form Precipitates, while Titanium acts as a Precipitation Seed.

Alloying Element	**% (by Mass)**
Carbon	0.03
Nickel	18.00
Cobalt	8.00
Molybdenum	5.00
Titanium	0.50

A substantial amount of work has already gone into understanding the precipitation process, such as its reaction rate, it's products, and the variables it affects. The aging process throughout time is shown conceptually in figure 6 [12].

The presence of precipitates inhibits dislocation motion at grain boundaries, lowering ductility and increasing tensile strength and fracture resistance substantially [12]. The chemical properties of precipitates are not necessary for continuing this research further.

The change in properties from the precipitation process is immense and causes maraging steel to be much more of a useful material than unaged martensite alloys. After aging, ultimate tensile strength, and elasticity are all changed, as shown in figure 7 [13]. For example, the described Marval-18 Maraging Steel used in VIRGO has a listed .2% yield strength of only 1080MPa before aging, only 60% of its value afterwards, 1786MPa [10].

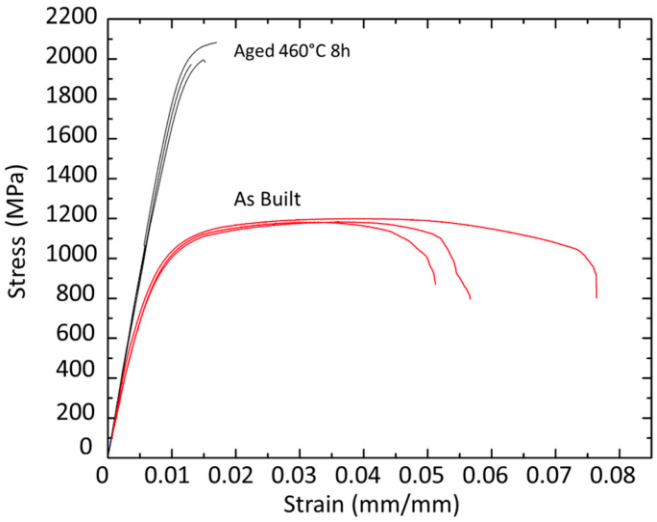

Figure 7. 18Ni Steel strain before and after aging. The net stress before yielding is nearly doubled, hardness increases, and the fractures becomes more pronounced [13].

Aging has some additional effects which may alter XRD results. During aging, a little Austenite (γ-Fe) reversion will also take place, particularly if typical aging durations are exceeded. Farooque et al. found that after 100 hours of heating at 485C, that nearly 20% of the lattice martensite irreversibly reverted to austenite in a maraging steel 350 [14]. In the much colder context, after 100 hours of aging at 435˚C, the precipitation process used for cantilever blades, only traces of Austenite are formed. As precipitates form during aging, a change is experienced in the concentration of alloy components within the martensite matrix. This can lead to a small change in the lattice constants of the martensite and be observed with XRD [15].

Aging is done during the manufacture, however to validate some results, samples are deliberately overaged. In the laboratory we use, a small DIY oven (figure 8) able to reach temperatures sufficient for precipitation hardening is utilized. While further aging steel samples which are already optimally aged accomplishes nothing, it will prove

useful to confirm that the observed differences in XRD are from residual stress and not from Austenite formation. This is based on the observation that relaxation of residual stresses ought not occur beneath resolubilization temperatures. ~ 580˚C [3].

Figure 8. A small oven linked to an argon tank. Samples are baked in a closed container sealed with thermal putty to keep the hot metal samples surrounded by an inert gas.

1.3 Corrosion of Maraging Steel

Corrosion is the destruction of a metal solid by chemical reaction through a series of Redox and often acid-base steps. This causes the metal to lose atoms to the production of an unwanted byproduct [16]. A significant amount of literature exists which describes the corrosion process of Maraging Steel already. Because it is an alloy, corrosion considerations apply to the basic α'-Fe lattice, as well as all the other elements which exist in maraging steel, largely as precipitates. For corrosion to take place, however, several reagents must be present; such as molecules in outdoor air at STP [16].

In the case of interest, with maraging steel blades under tension, the problem is exacerbated by small cracks. In crack tips which act as stress and strain concentrations,

the electrons bonding atoms are more energetic if strained [17]. This has the effect of reducing the energy potential barrier in the oxidation step for iron.

$$Fe(s) \rightarrow Fe^{2+}(aq) + 2e^{-}$$

The electrons ultimately find a compound to reduce, which can be take many reactions. In the case of maraging steel, hydrogen evolution is typically the main reaction [2].

$$2H^{+} + 2e^{-} \rightarrow H_2(g)$$

The hydrogen gas remains trapped inside maraging steel. Typically, the net result of the oxidation reaction will be fine, dark products containing the metal ions loosely attached to the surface. This thin layer of oxides will form on the surface until that layer passivates the metal from the corrosive environment; at this point the reaction slows to a negligible rate [16]. Under tensional stress, however, the corrosion reactions can proceed inside the cracks where water molecules can reach stressed metal, where the potential barrier in the oxidation step is lower. Thus, the rate of reaction increases according to Arrhenius' equation [17,18]. Understanding the full chemical reaction kinetics are not vital to the mechanism by which residual stress can improve the resistance of maraging steel to SCC.

1.4 The Mechanics of Solid Deformation

The distribution of stress and strain are necessary to describe SCC in bending blades. In general, strain in an arbitrary direction is denoted by ε and defined as

$$\varepsilon = \frac{\Delta l}{l_0}$$

And stress, σ, is a force per area through the material with units of pressure (typically MPa). By convention positive stress is tension and negative stress is compression [19].

$$\sigma = \frac{F}{A}$$

Both stress and strain are second rank tensors which operate on a fixed coordinate system to convey forces in every direction as well as shear factors which represent torques. It applies to an infinitesimal point inside the solid and is often quite different in different areas of the solid, depending on shape and loading.

$$\boldsymbol{\sigma} = \begin{bmatrix} \sigma_{11} & \sigma_{12} & \sigma_{13} \\ \sigma_{21} & \sigma_{22} & \sigma_{23} \\ \sigma_{31} & \sigma_{32} & \sigma_{33} \end{bmatrix}$$

Which is analogous to the stress state seen in figure 9.

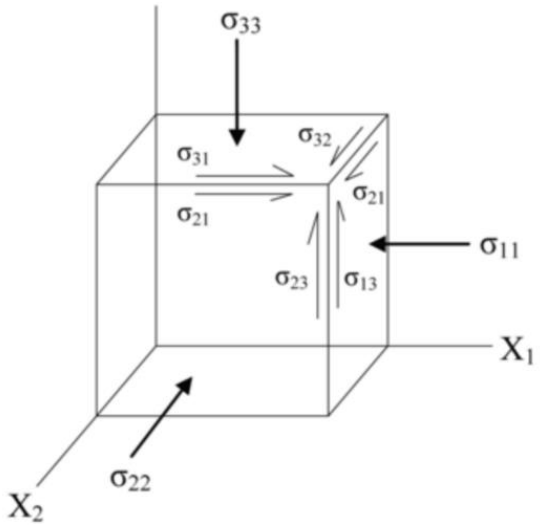

Figure 9. Stress tensor for a point. To keep a consistent frame of reference, x, y, and z are typically taken to be laboratory coordinates, or the edges of a rectangular solid. 1, 2, 3 are the directions of the principal planes and are typically solvable if the loading is known [20]

Fortunately, an easier treatment is attained by solving the eigenvalue problem for primary stresses, or "eigenstrains". The assumption here is that because the stress matrix is symmetric, that 3 eigenvalues of stress can be determined for a new coordinate system.

This has the effect of reorienting the stress tensor in the direction of the eigenvectors ($\hat{n}_i$) and diagonalizes the problem to a simpler expression [19].

$$\boldsymbol{\sigma} = \sum_{k=1}^{3} \sigma_i \hat{n}_i \otimes \hat{n}_i = \begin{bmatrix} \sigma_1 & 0 & 0 \\ 0 & \sigma_2 & 0 \\ 0 & 0 & \sigma_3 \end{bmatrix}$$

In the case that all three primary stresses are equal, the stress state is isotropic, spherically symmetric, and torqueless. For a case of bending, the three principal directions are easy to define for any point; one is the surface normal, one is along the bending axis and roughly equal to zero, and one in the bending direction which the highest value. Describing the strain response of the metal while undergoing loading and strain is complicated and depends on the material composition heavily. With no loss of generality, the strain tensor is related to a stress by

$$\boldsymbol{\sigma} = \boldsymbol{C}\boldsymbol{\epsilon}$$

And the term $\boldsymbol{C}$ is now introduced, referred to as material stiffness. Unfortunately, the requirement to relate two second rate tensors is a fourth rank tensor, with 81 terms. Symmetry in stress and strain tensors reduces the number of unique values to 36. Describing the entirety of this tensor is beyond the scope of this thesis, though lots of information is available in textbooks on material compliance.

The Poisson ratio, ν, relates the deformation in one direction, to resultant strain on the other directions in isotropic, linearly elastic materials [19]. In general, positive strain is stretching, and negative strain is compression; the same convention as stress. A unit cube aligned with the principal stresses will response to a compression in $\hat{1}$ with expansion in $\hat{2}$ and $\hat{3}$.

$$(1 + \epsilon_1)^{-\nu} = 1 - \epsilon_{2,3}$$

But often the relation is conveniently approximated for small strains.

$$\varepsilon_2 = \varepsilon_3 = -\upsilon\varepsilon_1$$

This does result in a small change in the volume of the unit as well, albeit negligible in this case. In the ideal cases where forces are axial in a single direction, the Young's Modulus describes the action [19].

$$\sigma_i = E\epsilon_i$$

1.4.1 Bending Mechanics

The maraging steel blades operate as cantilever beams, supported at an initial angle of ~ 45˚ with a vertical downward force at the tip [1]. The load experienced by the blade is static. Coordinate systems are defined in figure 10.

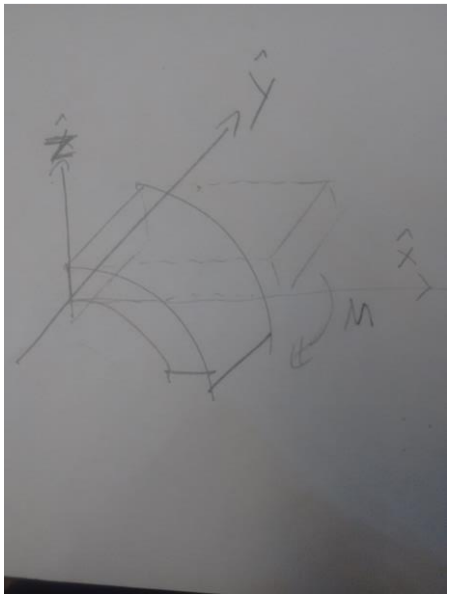

Figure 10. Coordinate system for bending

Predicting the displacement of a beam from bending requires solving the elastic curve equation, a second order ODE [19]. The beams for this chapter are given the coordinate system that is defined by figure 10. Bending is about the y axis, with displacement in z.

$$\frac{d^2z}{dx^2} = \frac{M_y(x)}{EI}$$

Which will yield an equation of $z(x)$, the downward ($\hat{z}$) displacement of the beam as a function of it's x coordinate. Bending can place different distributions of stress and strain inside materials, and how the load is applied, as well as the support points (boundary conditions to the ODE) determine the distribution. The case of pure bending is convenient, and applicable for reasons that will become clear.

After the equation is integrated, assuming the bending moment, $M_y(x)$ is known, it is possible to solve for strain using geometry from $z(x)$. From the picture, strain will be directed along the $\hat{x}$ direction. None is expected in $\hat{y}$ or $\hat{z}$, and the magnitude of strain will depend on the distance from the neutral axis, z. Solving the pure bending case where $M_y(x) = const$ yields the case in figure 11.

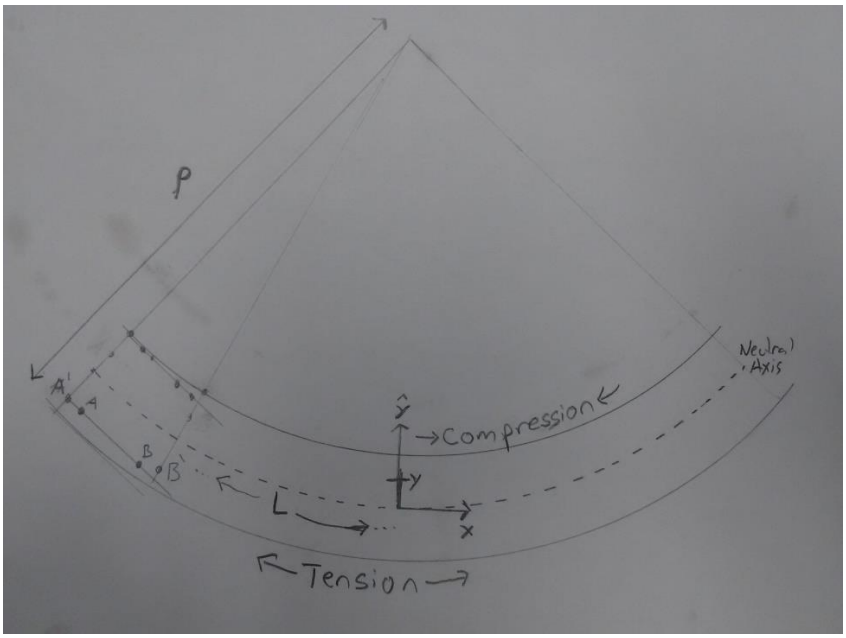

Figure 11. Calculation of strain in a pure bending beam

Before bending, the length in $\hat{x}$ of an infinitesimal beam segment is constant throughout the width and height of the beam; this length is denoted $\overline{AB}$ before bending, and then length $\overline{AB}'$ after loading. Referring to the picture, arclength

$$\overline{AB}' = (\mathrm{R} - \mathrm{y})\theta$$

And since the neutral axis has not elongated anywhere,

$$\overline{AB} = \mathrm{R}\theta$$

Then the tangent strain is given by

$$\varepsilon_{AB}(z) = -\frac{z}{\rho}\,\widehat{AB}$$

And the stress is

$$\sigma_{AB}(z) = -\frac{zE}{\rho}\,\widehat{AB}$$

ρ is the bending radius. This result is precisely what was expected: that stress increases linearly to the surfaces of the beam. At the outer faces, $z = \frac{\pm T}{2}$ and it corresponds to the maxima of compression and tension, respectively (fig 12).

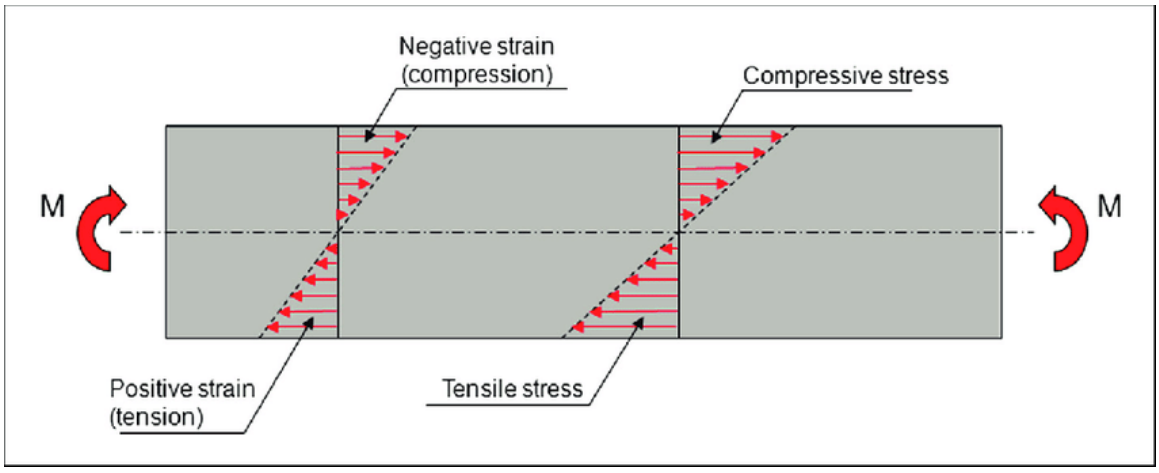

Figure 12. Linear increase in stress against height z of a beam [21]

Figure 13 is a demonstration of stress in a pure bending specimen, as generated through FEM simulations. It too demonstrates a uniformity of stress state along x and y, with the linear dependency in z. The color scale shows stress in the σ_{xx} direction only.

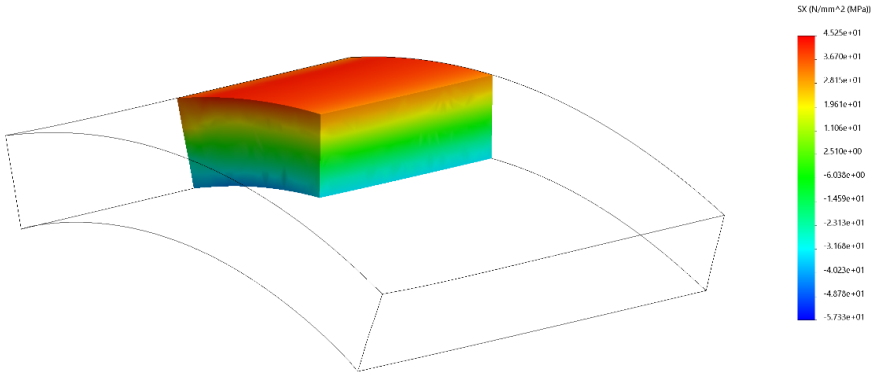

Figure 13. FEM Simulation of an alloy steel strip under pure bending. Results show stress in the x (lengthwise) direction. Units can be considered arbitrary.

The findings in this thesis apply to any region of bending where a tensile mode 1 force overlaps with the residual stress. Cracking will simply occur at the region of maximum tensional stress.

1.4.2 Fracture Mechanics

Focus was paid to the σ_{xx} because that force is responsible for the breakage of the maraging steel blades. Figure 14 shows the three modes of cracking which can occur, however since all maraging steel blade failure cases were mode 1, that will remain the sole focus. This makes sense given how the loading leads exclusively to $\hat{x}$ tension with little to no shear [19].

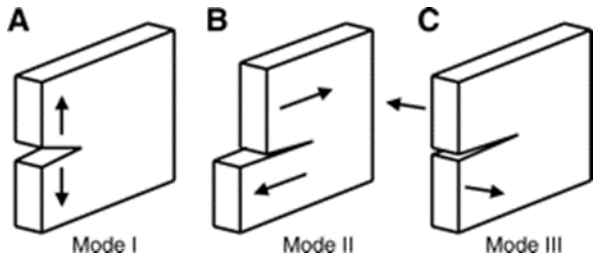

Figure 14. Three modes of cracking. Mode 1 arises from tension, modes 2 and 3 are caused by shear forces.

Previous sections made no mention of breakage or the plastic limit. All blades only operate within the elastic range of the material, where stress and strain are related linearly by Young's Modulus, E [20]. However, all materials have a limit after which the applied stress causes the units to deform plastically. This is the case where a paperclip, bent by hand, does not return to its original shape; maraging steel blades exhibit little of this behavior in the elastic region but then yields smoothly when the plastic regime is exceeded [22].

The stress intensity factor K is typically used to describe the state of stress concentration directly beneath a crack, where propagation will continue.

$$\sigma_{xx}(z) = \frac{K_I}{\sqrt{2\pi z}} f_{ij}(\theta)$$

Clearly this function is asymptotically infinite at $z = 0$, which is at the crack tip, and falls off in every direction. It by no means represents the true stress state in the solid because plasticity happens near the crack's tip to limit stress; however, it, serves a purpose in comparing different geometries and serving as a reference [21]. Predicting K in an actual sample, depends heavily on the geometry of the beam in consideration and the microscopic stress distribution; this is typically not feasible and not necessary for this thesis. For the case of pure bending, however, derivations have existed for some time

and provided the basis for figure 15, which shows the stress beneath a crack. For cracks of depth a with a total depth w the function is defined the following expression [23].

$$K_I = \sigma_{max}\sqrt{\pi a} \times f\left(\frac{a}{w}\right)$$

Where $f(a/w)$ is a geometrical factor and can be looked up in tables such as [23].

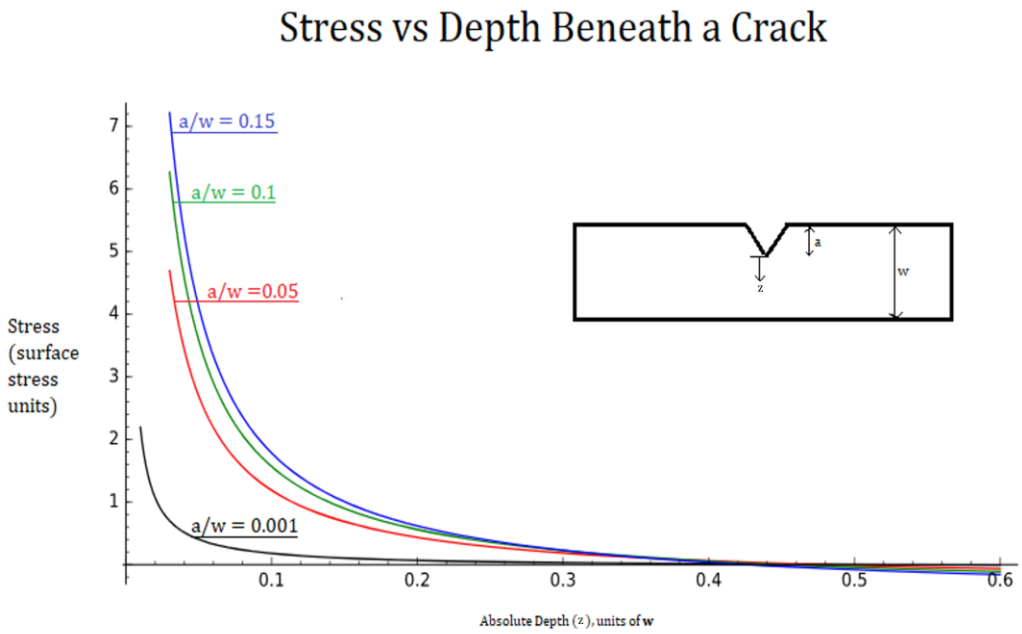

Figure 15. Stress distributions beneath a crack tip in pure bending. a/w is the percentage of the thickness that the crack has achieved.

When K_{IC}, the I standing for mode 1 and C denoting criticality is exceeded by K_I, the load stress intensity factor, then the crack velocity increases logarithmically, and the failure time is dramatically shortened.

$$K_I > K_{IC}$$

K_{IC} is also difficult to estimate with theory, however many measurements exist already for steels. As cracks propagate through the blade, the remaining thickness of material is reduced, and this places a higher stress at the crack tip; thereby having the effect of

raising K_I in the metal in a positive feedback loop. For high strength steels, this process happens very quickly and therefore a "snapping" kind of break is typically observed with no evident plastic behavior at all. Snapping never happens in maraging steel because it becomes super-plastic as soon as its elastic limit is achieved.

1.4.3 Stress Corrosion Cracking in Maraging Steel

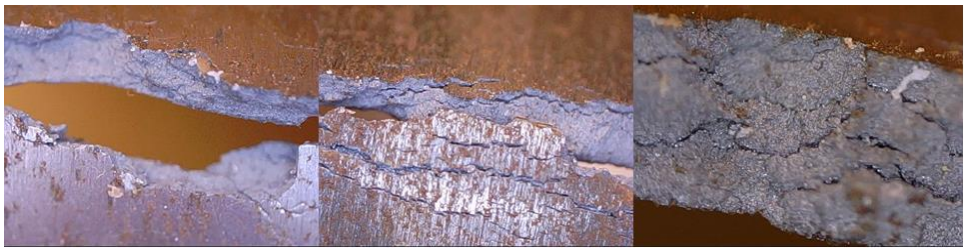

Figure 16. A mode 1 fracture in a maraging steel blade

Stress corrosion cracking in maraging steel is a similar phenomenon; however, the process is aided by corrosion reactions with water molecules taking place at the crack tips. A new, lower, stress intensity parameter K_{ISCC} is introduced which works identically with the brittle fracture parameter [17]. That is, logarithmic crack propagation acceleration is observed when

$$K_I > K_{ISCC}$$

Note that $K_{ISCC} < K_{IC}$ and that corrosion resistant metals tend to have very similar values for those two parameters $K_{ISCC} \approx K_{IC}$. Very susceptible materials have significantly different values $K_{ISCC} \ll K_{IC}$, and require careful utilization. Predicting K_{ISCC} from theory and conditions is extremely difficult to do, and values are almost always measured with experimentation [17]. The key point is that in Maraging, K_{ISCC} strongly depends on the availability of water molecules.

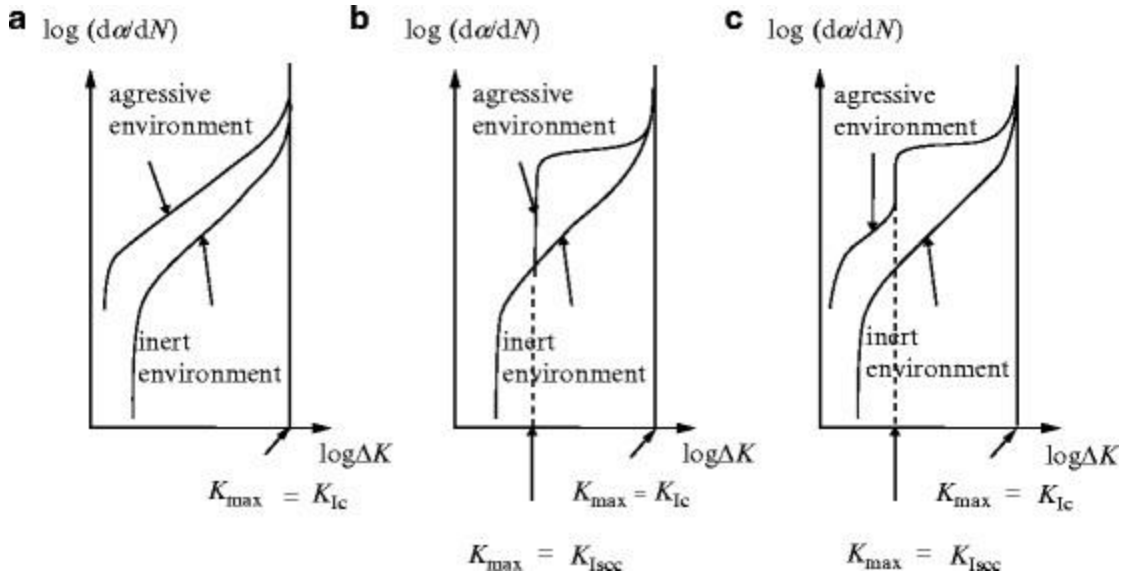

Figure 17. Crack velocity for stress intensity factors in three SCC behaviors. [17]

From literature, typical K_{ISCC} values for maraging steel 250 were in the range of 15-30 with the higher strength steels being even more susceptible [17]. An approximation to determine the depth of a crack in which the stress is sufficient to reach K_{ISCC}; is defined in [17]

$$a_{cr} = .2\left(\frac{\sigma_{.2y}}{K_{ISCC}}\right)^2$$

This formula yields a theoretical critical crack depth of $1.42\mu m$ for a maraging steel with $K_{ISCC} = 15$; this is a worst-case scenario. In an optimistic context, a $K_{ISCC} = 30$ suggests a critical crack depth of $5.68\mu m$. If the compressive residual stress neutralizing the bending stress the cold rolled blades penetrates at least to these depths the material becomes stress corrosion resistant.

The energy levels of the metallic bonds at the crack tip, which participate in the corrosion reaction, are increased by the presence of strain. As a result, the energy barrier for the oxidation step is reduced and the reaction rate for the corrosion reaction

accelerates. According to Hooke's Law, the energy stored by stretching is proportional to displacement squared, and this is why stress corrosion is more dangerous than cases in vacuum [17].

$$\Delta E \sim \varepsilon^2$$

When the blades are loaded, if the residual stress is neutralizing part of the load stress at the crack tip, the corrosion rate is reduced an amount proportional to the square of the change in strain, which can be quite significant.

1.5 Residual Stress

Residual Stress is one of the more intuitive topics covered in this thesis, defined as the stress $\boldsymbol{\sigma}_{res}$ which exists in a stationary solid, even when the metal is not externally loaded [19].

The profile of these stresses can be manipulated and controlled for beneficial use depending on how they are created; naturally a great deal of information and literature is available on the subject [3]. Among these are methods are quenching, etching, peening, and cold rolling, which is shown in figure 18.

Figure 18. A commercial cold roller in a steel factory [25].

This experiment concerns itself with the residual stress in *cold rolling* process; thin sheets of metal are repeatedly squeezed between rotating drums, until the thickness of the metal is permanently reduced by plastic deformation, like figure 19. This squeezes together the grains on one scale and breaks them, but also permanently compresses adjacent atoms within the grains to produce a strain field [26]. The atomic bonds end up permanently deformed especially at the surface where the deforming forces are applied, leaving some strain $\boldsymbol{\varepsilon_{res}}$, and a corresponding residual stress in the restoring force direction. Often the crystal grains are also beneficially affected being reoriented into a more favorable configuration for mechanical use [3]. Hardness, surface smoothness, and tensile strength are increased as a result, though it comes at the expense of ductility [3], but this is not relevant here.

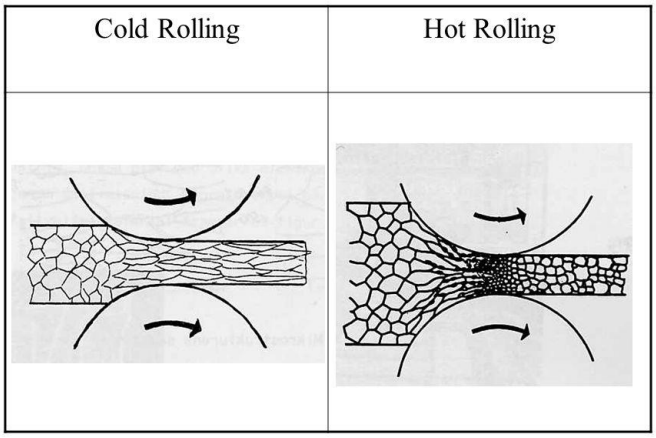

Figure 19. Differences in crystal grain orientation between hot and cold rolling. Hot rolling allows crystals to reform after they are compressed, leaving little or no residual stress.

For cold rolling the tendency is clear: outer faces of the steel carry a compressive residual stress while the center is under tension [3,27]. The depth stress profile in a solid

material is difficult to determine non-destructively; and can vary significantly depending on small changes to input parameters. Similarly, to predict the stress profile leftover after a cold rolling operation requires a lot of information about that manufacturing process [27]. Figure 20 shows an arbitrary residual stress which represents the general trend that surface compression is high near the surface, while in the middle is a larger thickness of lower amplitude tension.

1.5.1 Measuring Surface Residual Stress Using X-Ray Diffraction

X-Ray diffraction is a relatively simple, non-destructive technique to measure the residual stress at the surface of a solid sample, and this may be sufficient to prove the existence of compressive residual stress in the cold rolled samples [28]. Therefore, this technique can be useful in trying to predict a metals possible corrosion resistance.

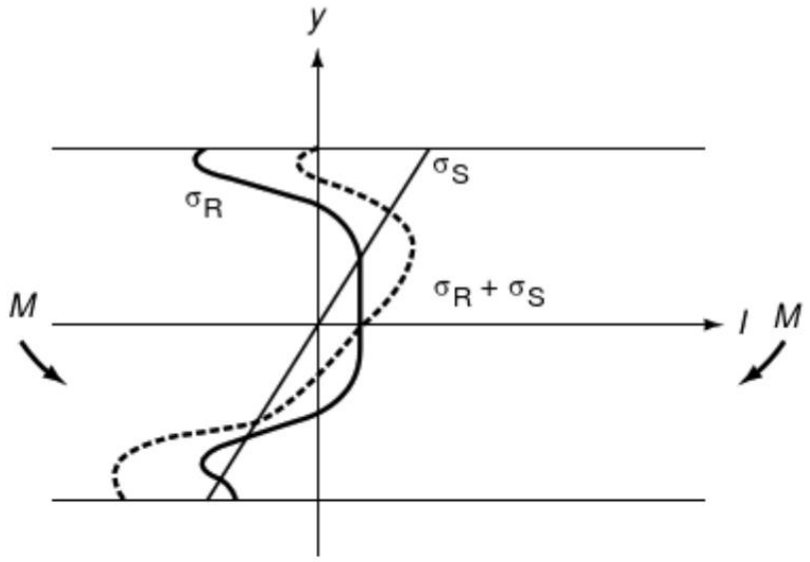

Figure 20. Sum of mode 1 stress vs depth in a cantilever beam subject to a bending moment M. The straight line is the stress profile on a blade that has no internal stresses before loading. The dark line is the residual stress profile typical of a cold-rolled blade, the dotted line is the stress profile of a cold-rolled blade subject to a bending momentum load. Note how the stress corrosion inducing tensional stress at the upper surface is nulled, thus inhibiting initiation of crack propagation.

1.5.2 Stress in a cold-rolled metal sheet

Newtons laws dictate that the sum of forces acting on a body describe its consequent motion. This also applies to elements within stress tensors of a common coordinate system inside a body [40], neglecting cases of hysteresis.

$$\boldsymbol{\sigma_{net} = \sigma_{res} + \sigma_L}$$

Figure 20 shows the biaxial stress in the bending direction of a pure bending unit; as the sum of load and residual stress. At the top surface, under greatest tension from bending, the net stress is zero due to the residual stress.

Ideally, the profile of samples can be measured through the entire thickness, though this is often not possible. Note that the only region of real importance is the upper surface where cracks initiate, since critical crack depth is very short and the center and bottom faces experience little or no tension required for mode 1 cracking.

1.5.3 Cold Rolling in the lab

To produce cold rolling for validations, a laboratory cold rolling machine is utilized, as shown in figure 21.

Figure 21. A small, table mounted hand-crank rolling machine

These samples are referred to as Lab-Rolled (LR), though the effect is still cold rolling. Industrial cold rolling is often done at several hundred ˚C [3], so while it is still cold relative to "hot" rolling, the effect from room temperature rolling in lab may be somewhat different. The lab roller is more uniform in applied force than commercial rolling machines but produces smaller "broken" crystals, due to the lower ductility at lower temperature. It is expected to be effective in imparting a compressive residual stress in maraging steel strips but perhaps with different XRD behavior than commercial cold-rolling, due to the temperature difference [3].

1.6 Crystal Structure of Martensite

The crystalline nature of martensite has already been mentioned, though not sufficiently to discuss the measurements of surface residual stress. Consider figure 23 showing three basic "cell" geometries which can form inside crystallizing matter. These unit cells repeat in every direction up until grain boundaries and comprise most of the solid alloy [7]. These crystals are by no means perfect; in addition to grain boundaries, within each grain are imperfections, dislocations, voids, and especially precipitates, which affect the mechanical properties. Most room temperature irons exist in the FCC, austenite phase, or with carbon in the lattice forming Fe_3C; Maraging steel is a Body Centered Tetragonal (BCT) lattice [7].

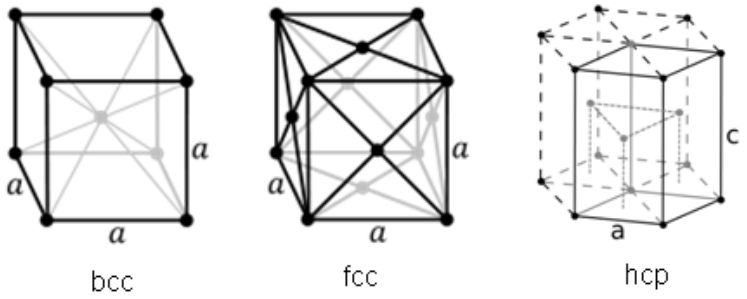

Figure 22. Lattice Geometries. Martensite is approximately a bcc crystal.

Martensite is made by rapid cooling once below a threshold temperature, often with water, which forces a transformation from FCC to BCT [7]. These lattices are defined by the Bravais Vectors below in table 2. While the true description of Martensite is BCT, it is very similar to BCC geometry with one-dimension c slightly longer than the others, a. An approximate equation for the ratio of lengths is given by [29]

$$\frac{c}{a} = 1 + 0.045 \times (\%_{Carbon})$$

Which in this case for maraging steel with a maximum of .03% carbon suggests that $c = 1.00135a$. This figure is negligible in Maraging and can be assumed unity, having a minimal effect on results.

Table 2

Bravais Lattice Vectors for FCC and BCC Geometry Crystals.

$\vec{R} = n_1\vec{a}_1 + n_2\vec{a}_2 + n_3\vec{a}_3 \quad ; \quad (n = 1,2,3 \ldots.) \; ; \; \{i, j, k\}$	
BCC	**FCC**
$\boldsymbol{a_1} = \frac{a}{2}(-\boldsymbol{i} + \boldsymbol{j} + \boldsymbol{k})$	$\boldsymbol{a_1} = \frac{a}{2}(\boldsymbol{i} + \boldsymbol{j})$
$\boldsymbol{a_2} = \frac{a}{2}(\boldsymbol{i} + \boldsymbol{j} + \boldsymbol{k})$	$\boldsymbol{a_1} = \frac{a}{2}(\boldsymbol{j} + \boldsymbol{k})$
$\boldsymbol{a_3} = \frac{a}{2}(-\boldsymbol{i} - \boldsymbol{j} + \boldsymbol{k})$	$\boldsymbol{a_1} = \frac{a}{2}(\boldsymbol{i} + \boldsymbol{k})$

As the metal is stretched or worked in a direction, the exact spacing between the atoms in any direction, a_i may be increased or decreased, requiring energy. A restoring force in the opposite direction is created; if these displacements exist in a stationary object then its residual stress [3]. The restoring force is proportional to the displacement, typically known as Hooke's Law; in such a treatment for iron the above stiffness constant

is approximately $k_{eff} \approx 47.0\ N/m$ [30,31]. If enough energy is applied, the bonds can outright break releasing energy. Figure 24 shows the bond energy against bond length for iron in a BCC crystal, as an example [31].

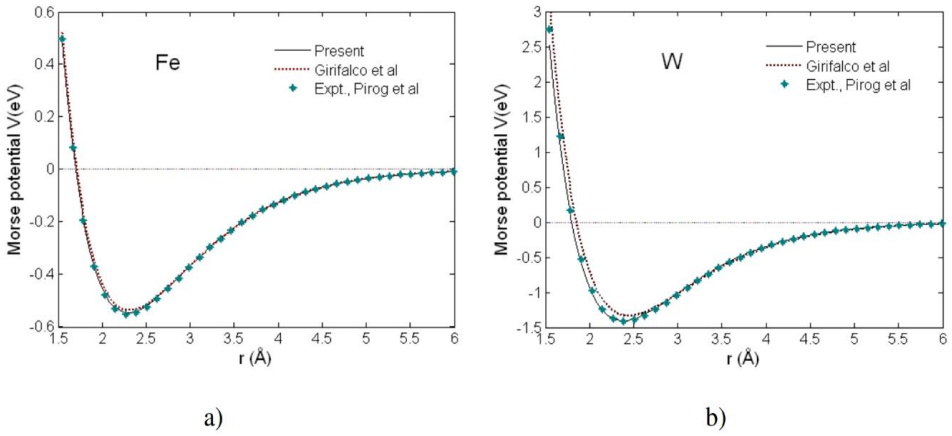

a) b)

Figure 23. Bond stretching energy approximates for Iron and Tungsten in BCC geometry. [31]

1.6.1 Miller Indices

Crystals can be rotated in any angle to view new planes facing parallel to a reference surface. These planes repeat with a regular frequency with a specific separation and are typically described by Miller Indices. A near-infinite number of such planes exist in a sufficiently large crystal. Three combined integers define a plane normal to the vector $\begin{bmatrix} h \\ k \\ l \end{bmatrix}$. By rearranging the values of h, k, and l, two identical planes are produced in 90˚ rotations; hence physics of 110 is typically treated as identical to 101 and 011 in cubic cases [32].

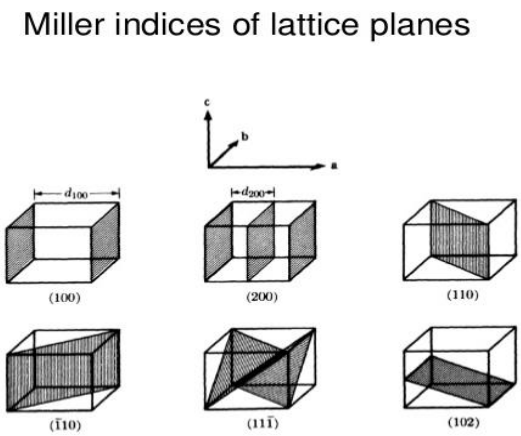

Figure 24. Crystal lattice planes in cubic geometry defined by the three miller indices.

1.7 X-Ray Diffraction

X-ray diffraction is a non-destructive method to measure lattice spacings near the surface of crystalline solids by utilizing the scattering of high energy radiation [33]. An X-ray source, Cu for these experiments, illuminates the sample with a beam. Much of the intensity undergoes specular reflection from the surface, reflecting off at the same angle as the incoming rays. A small amount enters the metal, scattering off atoms and a smaller amount still will exit at an appropriate angle to reach the detector [33].

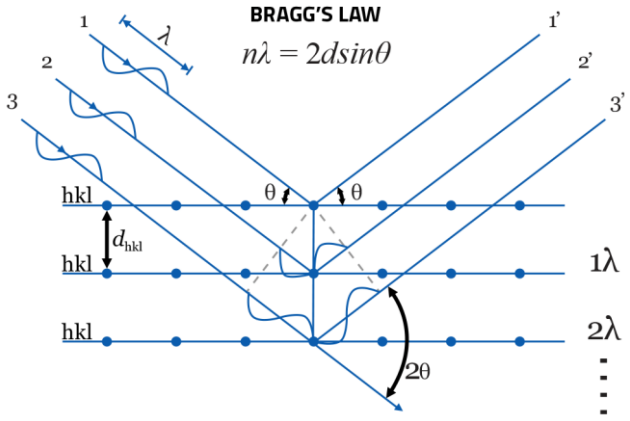

Figure 25. Bragg diffraction with X-Rays

All rays that exit from beneath the surface interfere constructively between planes only if the incoming and outgoing angles are such that the net path difference is an integer wave [33,34]. This is known as Bragg diffraction.

$$n\lambda = 2d_{hkl}\sin\theta$$

λ is the wavelength of the beam, and n is called order of interference and for the sake of this paper limited to cases of 1 because higher terms do not appear in the available hardware. The geometry of a cubic crystal is simple, and with the assumption of a bcc crystal the spacing can be determined by

$$d_{hkl} = \frac{a}{\sqrt{h^2 + k^2 + l^2}}$$

if necessary [38].

Scanning is done over a range of input and output angles to find those that produce constructive interference. The source and detector are angle-synchronized in the used diffractometer, a Bruker D2 Phaser (figure 26), primarily intended for powder samples. It is equally good for polycrystalline materials, which are effectively a sintered powder of crystals [34].

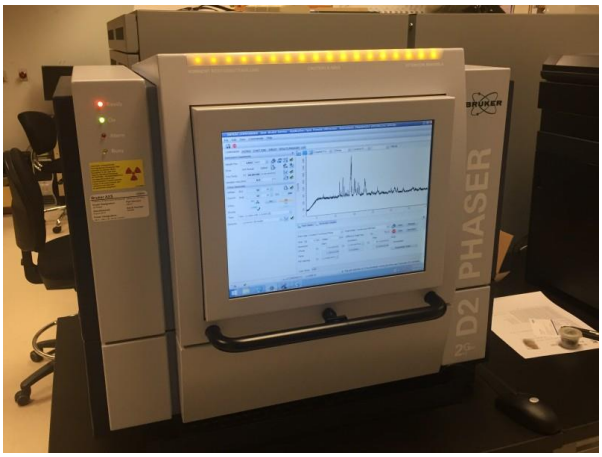

Figure 26. The Bruker D2 phaser

Detection is plotted against the deflection angle 2θ to extract the diffraction information from the intensity peaks; this is the data of interest.

Not all crystal planes will lead to constructive interference; the bcc lattice is limited to cases where the sum of the miller indices is an even number. For this reason, the maraging steel which is primarily iron, will only form peaks for (200), (110), (211), (220), etc. [35]. Planes with a larger sum of Miller indices are more difficult to detect. A hypothetical XRD pattern is shown in figure 27.

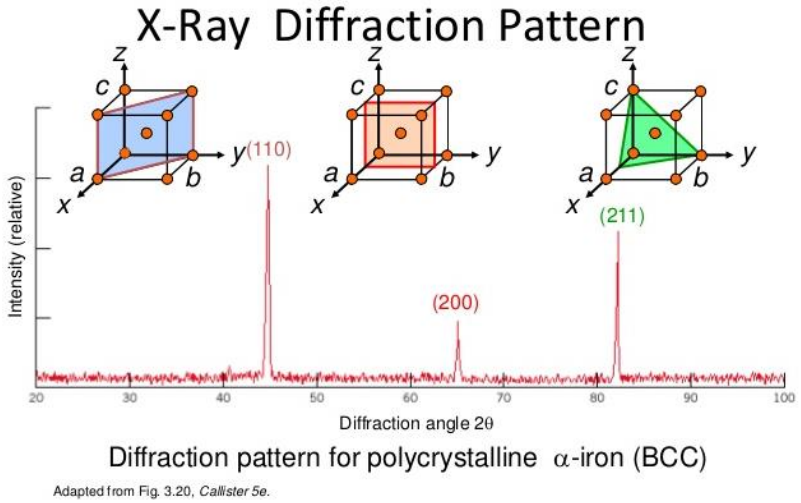

Figure 27. Sample XRD result for ferrite in a system using a Cu source.

The strain on one grain is assumed to be equal to the strain on other grains even if they are not individually measured. For a single piece of metal, billions of crystals in every orientation exist, and on any given surface all crystal orientations will be present; only a small fraction are aligned to participate to the measurements. Therefore, if the beam size from the x-ray source is sufficiently large, all possible planes can be considered to comprise the illuminated area and participate in diffraction [33].

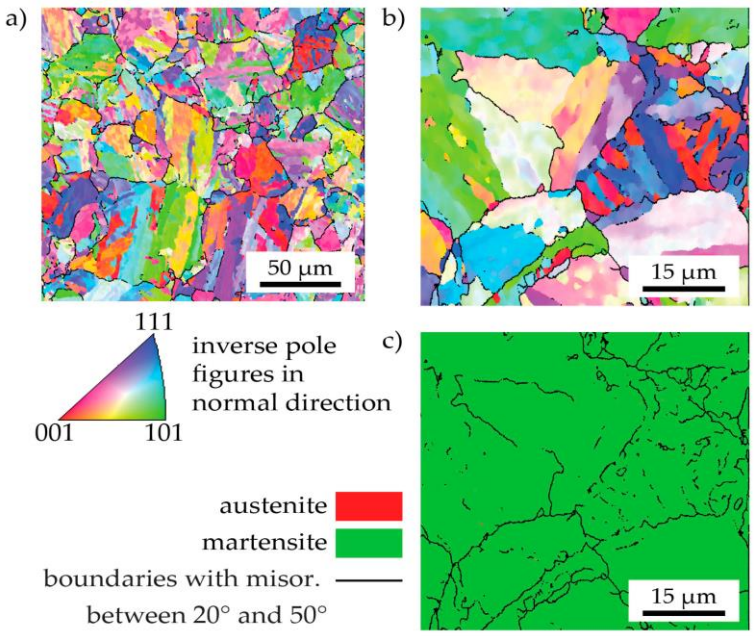

Figure 28. Pole Map of Maraging Steel [36]

1.7.1 Measurement Samples

The maraging steel samples are thin planes, cut into units roughly the size of a US quarter; though flat, no noticeable features are visible on the surface to suggest any preferred direction from rolling. Grinding direction is visible on the ground pieces, which could be used as a reference, though was never necessary and had no effect on the stress state. The necessary first assumption is to take the state near the surface of interest to be in a *planar stress* situation where the surface normal stress is zero ($\sigma_z = \sigma_3 = 0$), and thus merely biaxial in the other two; the normal strain however is still nonzero ($\epsilon_{z,3} \neq 0$) due to the Poisson module. The perpendicular (biaxial) coordinates abide by the convention that ($\sigma_1 > \sigma_2$) [33].

Figure 29. Two ground-to-thickness samples.

1.7.2 Determination of residual stress with XRD

If a metal undergoes compression or experiences any strain that affects the interplanar spacing d_{hkl}, it can be measured with XRD. The expectation for this experiment is that the surface-normal planes are squeezed together from cold rolling, which will cause an increase in the corresponding angle 2θ. Because of the linearity of Young's Modulus, this also makes predicting stress simple. This method for the determination of biaxial stress is the same as outlined in the *NPL Determination of Residual Stresses by X-Ray Diffraction Issue 2* [33]. The methods described there, however, were originally performed and derived by Lester and Aborn in 1925 [37].

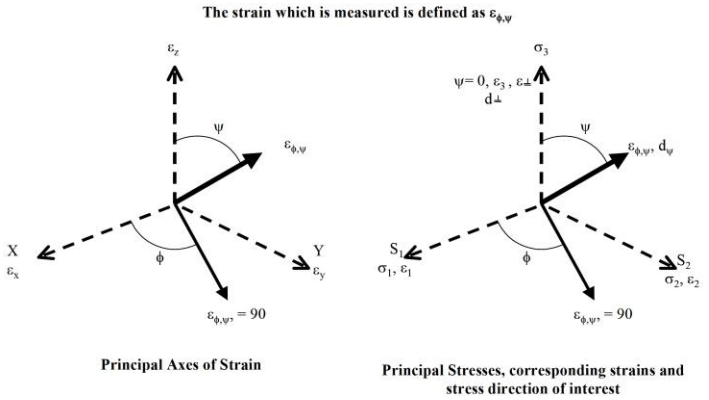

Figure 30. Coordinate system for determination of residual stress.

The previous section described ways that x-ray diffraction measures crystal plane spacing normal to a reference. In this system, we are using the 110 planes normal to the surface, measured with Bragg diffraction. The relaxed value of this spacing is not known and this will present a critical problem for the experiment later. Since normal stress and strain are not the figures of interest, ways to relate this to the biaxial stress are necessary.

Since the Bruker D2 powder diffractometer only measures surface normal strain, the longitudinal strain needs to be calculated. The constitutive relations approximately describe the force-reaction to the metal [33].

$$\varepsilon_1 = \left(\frac{1}{E}\right) * [\sigma_1 - \nu(\sigma_2 + \sigma_3)]$$
$$\varepsilon_2 = \left(\frac{1}{E}\right) * [\sigma_2 - \nu(\sigma_1 + \sigma_3)]$$
$$\varepsilon_3 = \left(\frac{1}{E}\right) * [\sigma_3 - \nu(\sigma_1 + \sigma_2)]$$

Since the normal stress σ_3 at the surface is taken to be zero, the stress is planar and the third equation reduces conveniently to

$$\nu(\sigma_1 + \sigma_2) = -E\varepsilon_3$$

No further information is known about the biaxial stress aside from the magnitude of their sum. If the two are assumed to be equal, the residual stress is predicted from the X-Ray measurement. Just as easily, one can estimate the ratio $\xi = \frac{\sigma_1}{\sigma_2}$ if enough information about the manufacturing process is available. No reliable source had a consistent answer for cold rolling of maraging steel, though a recent experiment yielded $\xi = 1.25$ in a Ti–6Al-4V alloy [38]; most likely this property can be engineered for different use cases. For shot peening, this value is typically near unity [3]. Often, however, maraging steel is rolled in crossed directions; the Aubert Duval cold rolling

process is not fully known at present. Therefore, $\xi = 1$ is assumed for the results in this research.

To experimentally determine the complete stress states in the surface tangent directions, controlled tilting and rotating of the sample (or reference plane of the source and detector) would be necessary in ψ and φ respectively. If $\sigma_3 = 0$ then at any orientation of the sample in those angles, the measured strain is defined in terms of the principal stresses with the following equation [33].

$$\varepsilon_{\psi\varphi} = \frac{\Delta d_{\psi\varphi}}{d_{0,\psi\varphi}} = \frac{1+\upsilon}{E}(\sigma_1 \cos^2\phi + \sigma_2 \sin^2\phi)\sin^2\psi - \frac{\upsilon}{E}(\sigma_1 + \sigma_2)$$

And rearranging terms yields

$$\sigma_\varphi = \frac{E}{(1-\upsilon)\sin^2\psi}\left(\frac{d_\psi - d_n}{d_n}\right)$$

The Bruker diffractometer does not enable azimuthal tilt in ψ. Only planes normal to the sample surface could be measured and thus neither ψ nor φ are significant for any calculations [33].

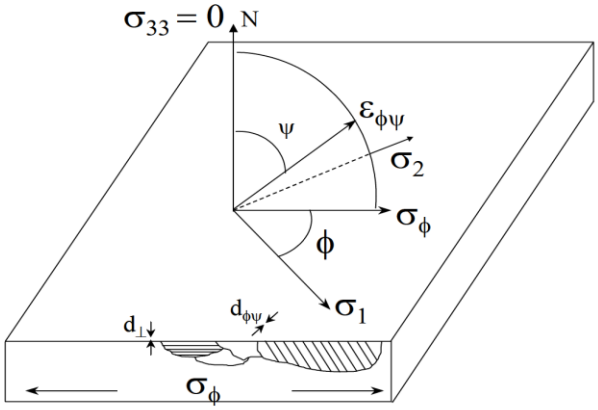

Figure 31. X-Ray diffraction measurements for different angles of ψ, φ

A peak broadening effect is expected in samples that are cold rolled; this behavior is described by the Scherrer equation. Quantification of crystallite size τ is done by studying the FWHM of a peak, β, while K is a shape factor generally assumed as unity [33].

$$\tau = \frac{K\lambda}{\beta \cos\theta}$$

Wider peaks are due to the smaller size of crystal elements, and more of them participating in the diffraction. A pole map of the surface in a cold rolled maraging steel sample effect is shown in figure 32, which should produce consecutively wider peaks.

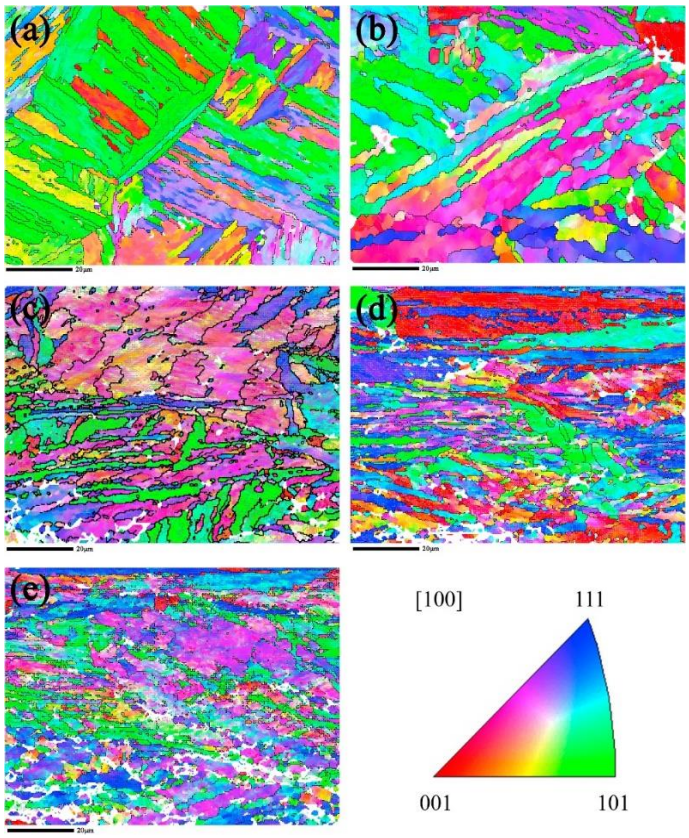

Figure 32. Crystal and fracturing orientation map for a Fe-Cr-Ni-Mo-Ti maraging steel after thickness reduction of: a. 0% b. 15% c. 30% d. 45% e. 60%. Smaller crystals result in a wider response in the X-Ray spectrometer signal [39]

CHAPTER 2

Results

Data collection began in Fall of 2017 using the Bruker D2 Phaser powder diffractometer. Dozens of Maraging Steel samples were available in 1x20x80mm strips for ground-to-thickness type, and 2.2x20x80mm for factory cold rolled units; several were pre-cut to match the x-ray diffractometer holder standards. Unless specified, all results are taken with the sample being automatically rotated in φ throughout scanning; this should not affect measurements of $\varepsilon_{\perp}$ because of the polycrystalline structure of the samples and increases the robustness of the measurement. The parameters of the x-ray diffraction were that of using a 3mm screen to prevent unwanted noise, using 1.2s/div integration times, and an angular resolution of $\Delta\theta = 0.01°$. The source was Cu with a crystal selected wavelength of $\lambda = 1.542\text{Å}$.

2.1 Initial Comparison

The first scan shows the full diffraction pattern for one of the ground to thickness units, as provided by Galli & Morelli (figure 33). Samples like this are identical to some units that failed in the VIRGO [2]. Two main peaks are visible in the XRD plot, one at $44.53°$ which is the α-(110) plane, and another is visible at $64.5°$ which represents the α-(200) plane; these are as expected. Scanning at greater or smaller deflection angles to detect more peaks is possible, but was found to be unnecessary in clean, unoxidized samples.

A small shape appears on the lower side of the α-(110) peak which is likely Austenite γ-(111). Some amount of it is always present in maraging steel, and more might have reverted during grinding, or that the figure measured simply represents a normal

quantity. Normally these γ-Fe (111) peaks are closer to ~43.5˚for similar setups, rather than the 44.3˚ that the gaussian fit measured [37]. However, a five DOF gaussian to account for tails placed the peak center at $2\theta_{\gamma(111)} = 43.8°$, which seems more reasonable; this is not shown on figure 33. The α-(110) is a better choice for studying strain due to its stronger signal; in every other way the α-(200), α-(211), or even α-(220) planes would be just as effective.

The ground-to-thickness sample is treated largely as a control; no other samples were available that had not been modified since the original cooling below martensite formation temperatures. Determination of the true relaxed plane spacings d_0 is possible by resolubilization i.e. heating and briefly holding the sample beyond 850˚C to revert to Austenite, and then back to Martensite, thereby relaxing all residual stresses before XRD. Doing so in the lab would have been possible, though it was decided to be unnecessary. This decision was made largely because of the tendency for residual stress to decay rapidly with depth, and the amount of metal that was ground from the surface being substantial. For this reason, the peak at 44.5˚ of this sample was used as a benchmark and will be superimposed on other XRD results for comparison.

The above assumption was probably partially unjustified, due to the cold-rolling stress profile of figure 21, and the fact that the amount of material ground off on each side is unknown. This may explain some of the confusing results yielding different stress values of different faces of the same sample discussed in chapter 2.

All ground-to-thickness samples were ground from the same sheet of the cold-rolled samples as delivered by Aubert Duval.

Throughout the project, scans were compared with a ground to thickness samples with no treatment 11 times. The main reason for this was to make certain that the instrument's calibration was not drifting, and the need to compare measured samples with the reference one in case of spectrometer drift. The results are tabulated and shown in table 3. These measurements serve as the reference for determining strain in compressed samples later.

Table 3

Results for Ground to Thickness Maraging Steel Samples

Date	$2\theta_{110}(^{\circ})$	$d^{\perp}{}_{110}(\text{Å})$
9.29	44.52	2.034
9.29	44.53	2.033
9.29	44.52	2.034
10.06	44.51	2.034
10.06	44.82	2.021
10.09	44.52	2.034
12.12	44.52	2.034
3.06	44.47	2.036
4.12	44.56	2.032
AVG	**44.55**	**2.033**
STDV	**0.097**	**0.0047**

From these measurements we concluded that the instrument was stable within 0.2%.

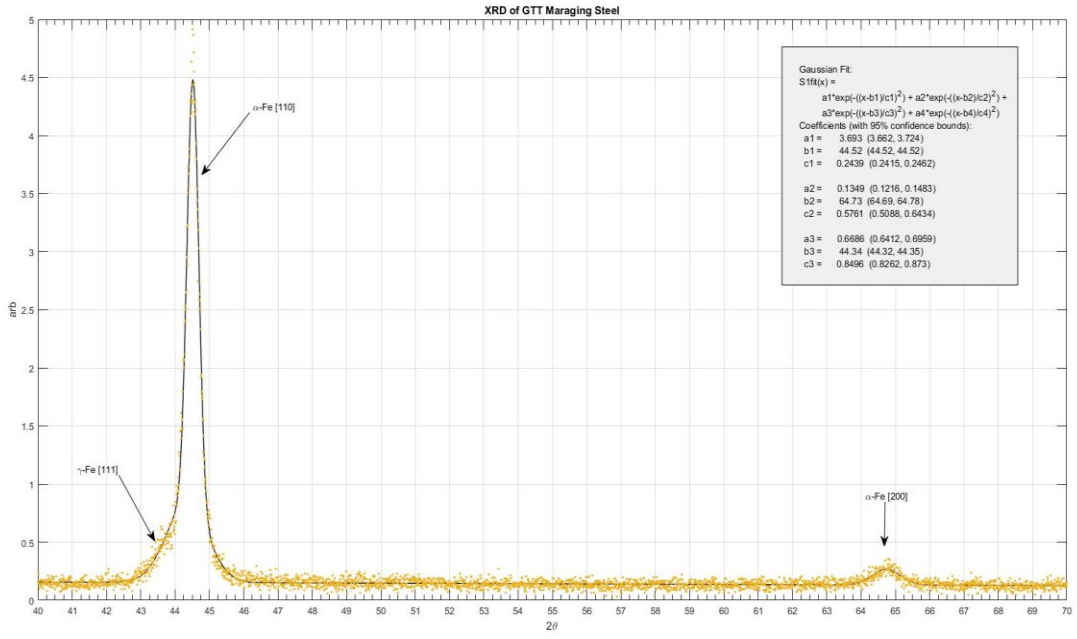

Figure 33. XRD result for Galli & Morelli ground to thickness pieces. Three peaks of note arise, with a small amount of austenite possible, nominally occurring at 43.5. The 110 peak at 44.52 Serves as a presumed standard relaxed lattice spacing d. This is mainly for comparison with other measurements later.

Figure 35 on the next page shows the diffraction pattern for a cold rolled sample as delivered by Aubert Duval, the original manufacturer. These pieces are expected to carry a residual compressive stress due to cold rolling they underwent during manufacture, and a correspondingly higher angle of α-(110) peak.

Several additional peaks are visible on the plot of the samples as delivered by Aubert Duval, which were not present in the ground to thickness samples. These are all explainable by the presence of oxides, products of oxidation, which were visible on the surface. Databases exist online which track XRD peaks [40], but in this case the peak amplitude reduction from a simple surface scouring test sufficed to identify them as surface oxidation residue. Most steels will slowly form a passive layer upon basic exposure to air and this is likely all that happened.

In figure 34, a scan of an Aubert Duval cold rolled piece before and after surface scouring clearly shows that the peaks at 37˚, 57˚, and 63˚ were surface features small enough to be attenuated by a light surface refinishing. The peak at 52.1˚ is most likely Austenite γ-(200), and no concern to the results.

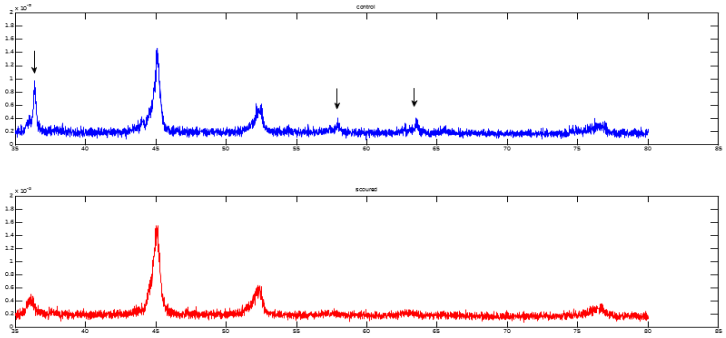

Figure 34. XRD patterns for Aubert Duval, cold rolled MS. Several peaks were significantly affected by a light surface cleaning treatment and do not represent any significant effect on the mechanical property of the steel. Interestingly, the α-200 peak is barely visible.

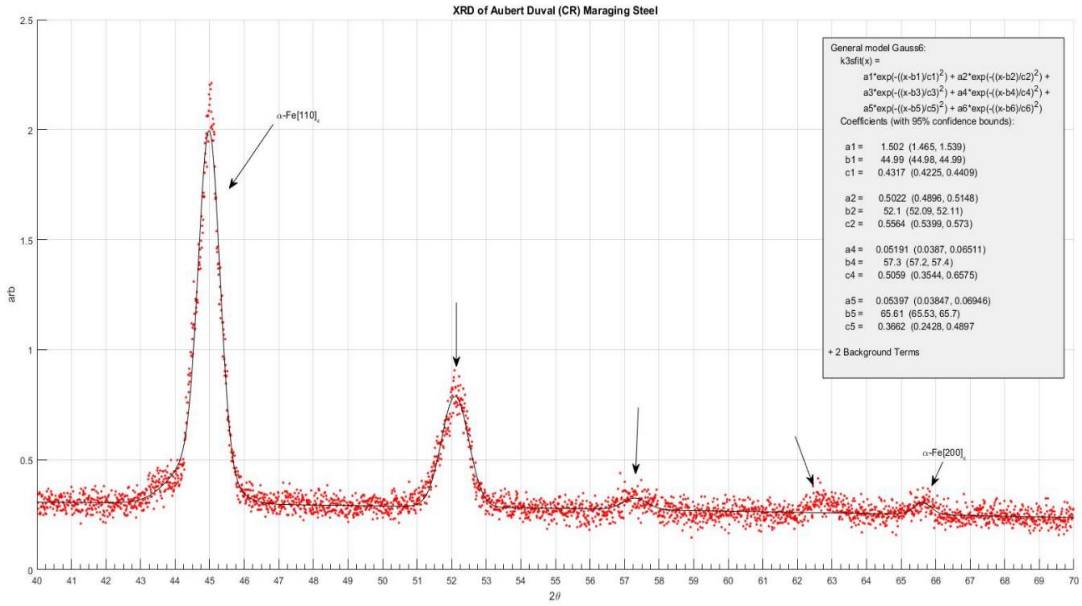

Figure 35. XRD of a maraging steel sample as provided immediately by Aubert Duval. This sample represents the fraction of maraging steel blades that did not break during operation. Most significantly, the α-(110) peak is located near 45.0 degrees which is a substantial move from 44.5 measured in ground to thickness samples from the same metal sheet.

Superimposed plots of the 110 peaks in ground-to-thickness and Aubert Duval cold rolled samples are shown in figure 36 for two samples each. The angles for α-110 in the two samples averaged to 44.56˚ degrees for the ground to thickness samples, and 45.05˚ degrees for the cold rolled sample. Also, of note is the substantial broadening of the α-110 peaks in cold rolled samples; this is not surprising given known behavior of cold rolling to smash crystallites into smaller fragments. Differences in amplitude are not significant, and merely represent differences in normalization due to the background.

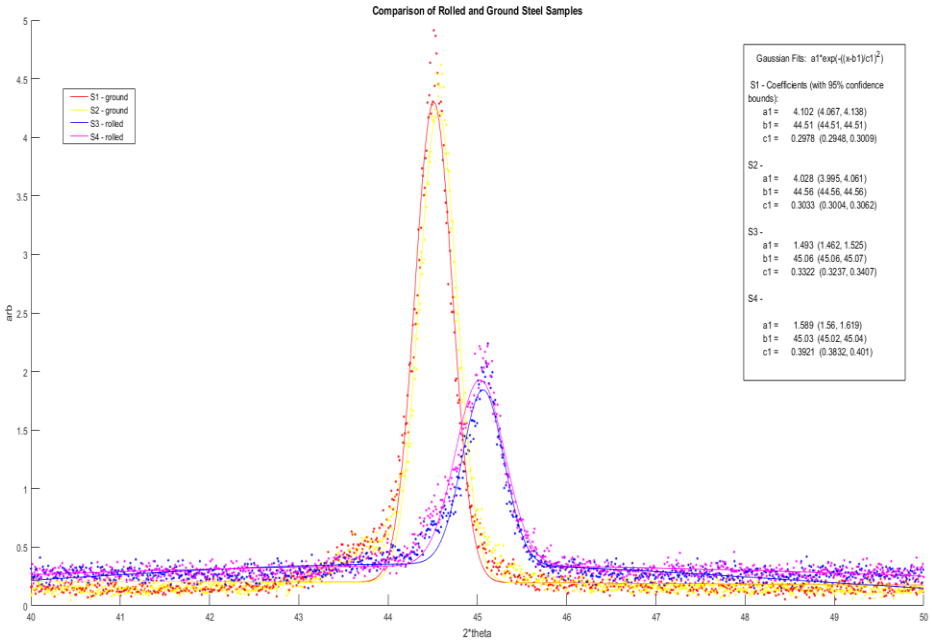

Figure 36. Superposed plots of XRD for 2xAD and 2xGTT Maraging steel α-110 peaks. Amplitude reduction does not reflect strain and broadening of the peak suggests potentially a reduction in crystallite size. The shift of peak to a greater angle suggests a compression.

Throughout the project, scans were completed on cold rolled samples with no treatment 6 times. The results are tabulated and shown in table 4. The most significant finding is that there is indeed a strain in $\hat{z}$ and therefore a stress in the biaxial directions. The magnitude of this stress can be evaluated from the strain and the Young's modulus

[33]. Biaxial stress based on the equations in sections 1.7.2 suggest a residual stress greater than yield; this is certainly not the real case. Instead, a baseline approximation is taken using the Poisson ratio and multiplying by a factor of $\frac{1}{2}$. Based on this criterion, the residual stress appears to be approximately -302 MPa which represents 16% of the listed ultimate tensile strength of 1850 MPa. This may indeed be sufficient to explain the survival of the cold rolled blades while ground to thickness or resolubilized units failed.

Table 4

Results for Aubert Duval cold rolled Maraging Steel Samples

Date	$2\theta_{110}(^{\circ})$	$d^{\perp}{}_{110}(\text{Å})$	$\varepsilon_{z,\perp}$	$\sigma_{xx} = \sigma_{yy} \approx \frac{-(\sigma_{11} + \sigma_{22})}{2}(MPa)$
10.02	45.06	2.011	-0.01070	-298.4
10.02	45.05	2.011	-0.01049	-292.6
10.09	45.06	2.011	-0.01070	-298.4
10.09	45.03	2.012	-0.01007	-281.0
10.09	45.07	2.010	-0.01090	-304.2
3.23	45.13	2.008	-0.01215	-339.0
AVG	**45.07**	**2.011**	**-0.01083**	-302.3
STDV	**0.03091**	**0.001306**	**.000643**	17.93

From this point onward, data plots are restricted to angle ranges of 40-50˚ which is more than sufficient for studying changes in the α-(110) peaks. This saves a significant amount of machine time, without taking unnecessary data.

It was tested that the peak shift survives the precipitation hardening process, as discussed in section 2.3.

2.2. Lab Cold Rolling

While the presence of a surface-normal strain does suggest residual stress is present according to the constitutive equations, there is an experimental way of confirming that this is the case. One needs to check that a peak shift can be induced with cold rolling in ground to thickness samples. This would prove that the residual surface stress is due to cold-rolling strain.

A test to confirm the existence of compressive residual stress from cold rolling was done in the laboratory using the crank-roller in figure 21. Several ground to thickness samples were rolled in the lab machine until ~25% reduction in strip thickness was achieved. This was done with cold rolling in only one direction, the strip-lengthwise. This took roughly 30 passes for each sample flipping the orientation of the sample between each pass to ensure symmetry of the stress state.

The result for one such unit is shown in figure 37. The lab-rolled piece presented an α-(110) peak now at $2\theta = 45.33^{\circ}$ which corresponds to a uniform biaxial residual stress of -454.2MPa. A slight but nontrivial broadening of the peak manifests as well, though this is expected from crystal fracturing. It is not surprising that we achieved greater apparent residual stress in the lab samples as compared with Aubert Duval's because this rolling was performed at lower (room) temperature [27]. It is also not surprising that the strain of 1.4% exceeds the ~1% limit on macroscopic samples. Likely, the profile beneath these two surfaces stresses is similar to that of figure 20, but proportionally different.

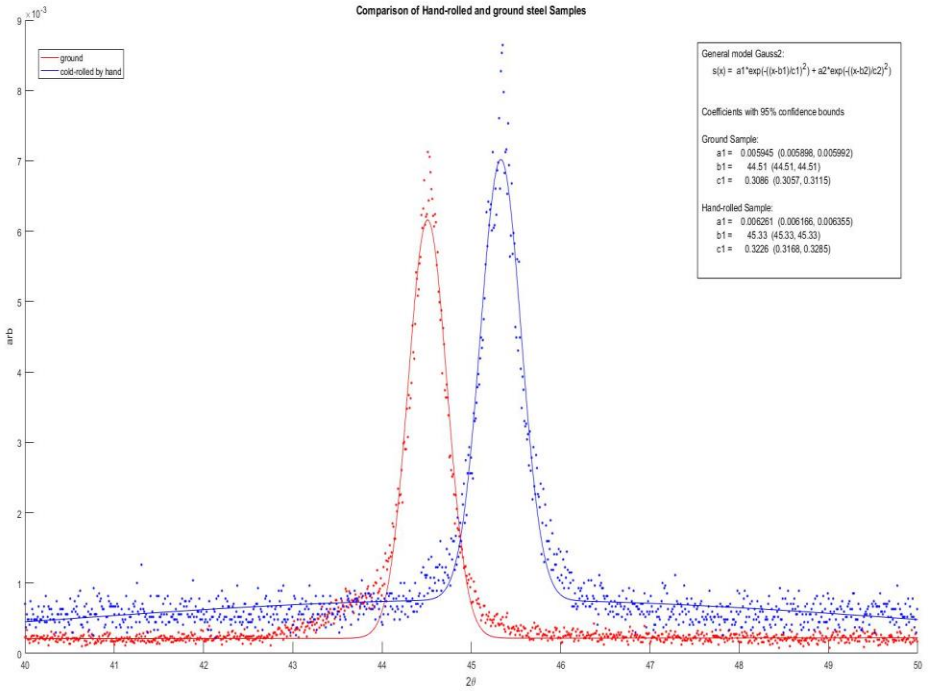

Figure 37. The diffraction result for a control GTT piece, and a GTT piece which was cycled through the roller until a thickness reduction of 25%

As an additional measurement, the cold rolled samples were diffracted on both sides, and in two perpendicular directions with the auto-rotate turned off. The results agree with the expectation that the measured strain should have no dependency on the planar rotation φ because the residual bidirectional stress is due to the Poisson's module-induced stress exceeding the plasticity limit during compression. Angle with respect to rolling direction had no effect on the XRD result, even though different stresses still exist in those directions [33]. Interestingly, one side of the sample appears to have achieved a greater normal strain than the other. This may be due to a small amount of asymmetric residual stress left by the original asymmetric grinding to thickness.

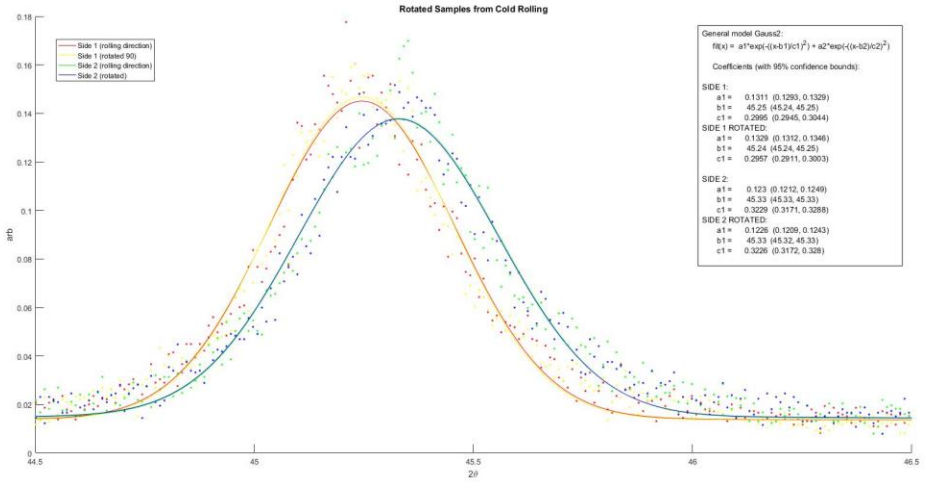

Figure 38. Four orientations of a same LR sample. Strain measurement appears to have no preference for orientation (as $\psi = 0$) but a slight inequality based on the sample side.

2.3 Surface Stress Surviving the Precipitation Hardening Process (Over-aging)

Using the jewelry oven in figure 8, the samples are heated to precipitation temperatures which, while substantially hotter than STP, do not reach recrystallization temperatures able to relax residual stress of steel. For a noticeable relaxation to take place, temperatures would need to exceed at least 580˚C for several hours [7]. The

experiment was done twice, the first time being at 480˚C and the second at 435˚C which is the manufacturer-prescribed aging temperature.

- 435˚C GM Ground-to-thickness 100hrs. (control) [fig. 39]
- 435˚C AD (CR) 100 hrs. [fig. 40]
- 435˚C GM Lab-Rolled 100 hrs. [fig. 41]
- 480˚C AD (CR) 100 hrs. [fig. 42]
- 480˚C GM Lab-Rolled 100hrs. [fig. 43]

Figure 39 presents the results of heating a ground-to-thickness control piece to 480C for 100 hours. The single α-(110) peak has migrated slightly to a wider 2θ angle, and the austenite γ-(111) peak has become much more prominent. None of this is unexpected or bad, even the specification sheet from Aubert Duval warns a small contraction of .05% can occur during aging [10], when Cobalt, Nickel, and Molybdenum exit from the solid solution to form the precipitates. The primary matter of focus here is that the "relaxed" α-(110) peak is not significantly affected by further aging. Following the control, units with predicted residual stress are tested; α-(110) peaks will ideally not move, though a small change is inevitable particularly for 480˚C aging.

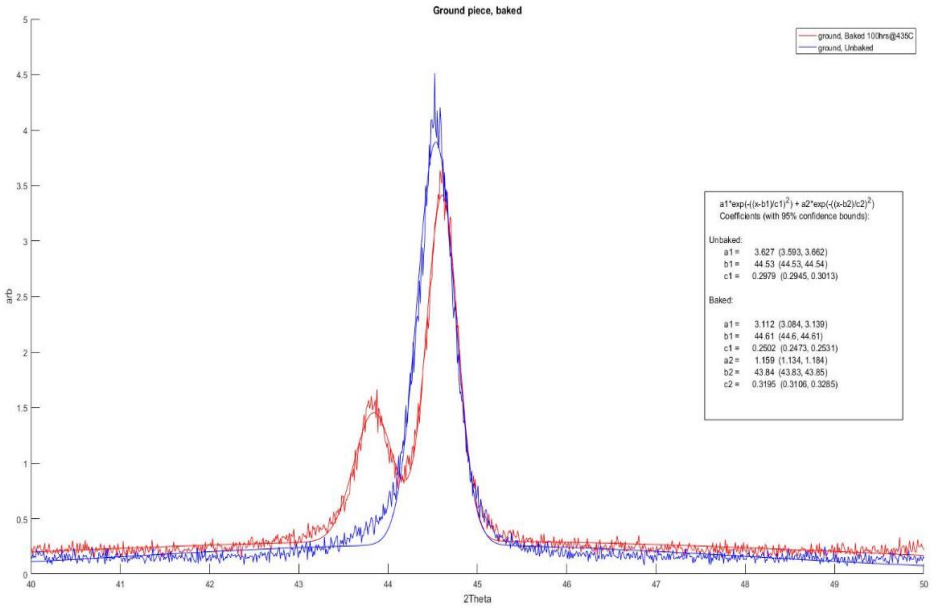

Figure 39. XRD of a ground-to-thickness piece before and after heating for 100 hours at 435C

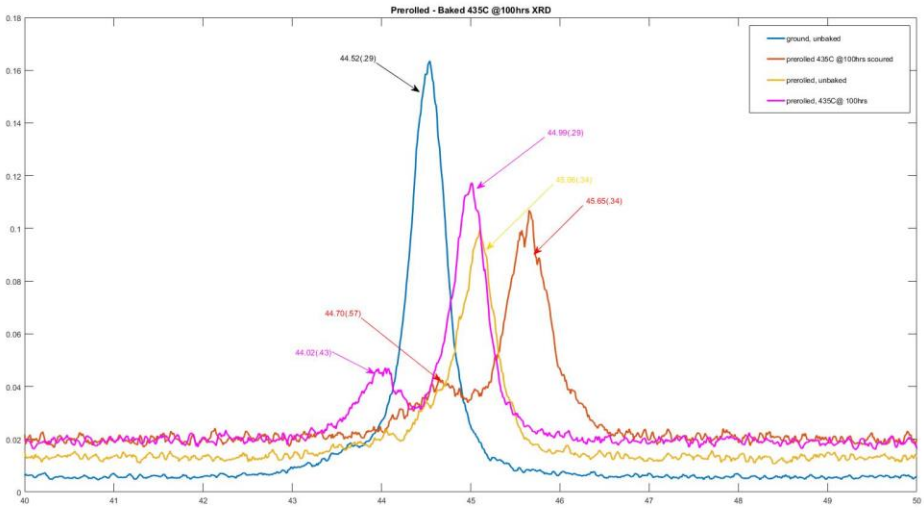

Figure 40. Aubert Duval cold rolled Piece before and after aging at 435C.

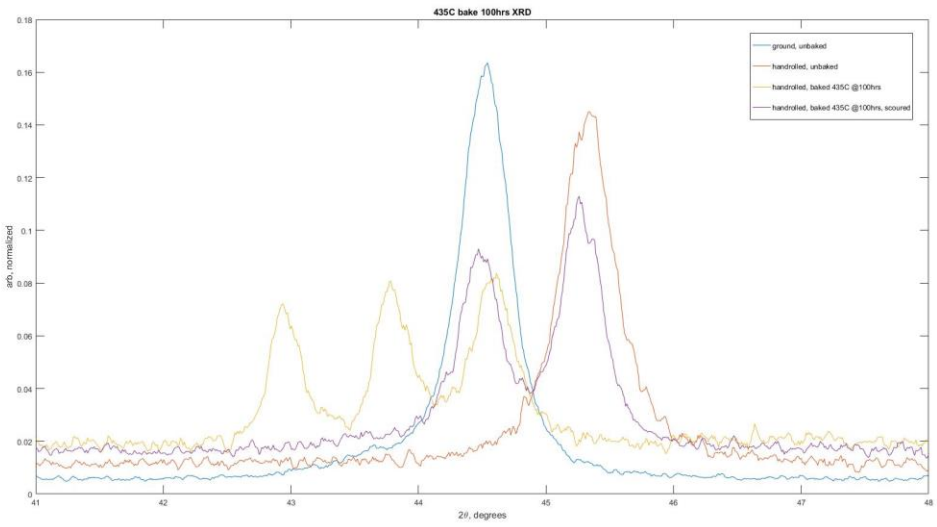

Figure 41. Lab-Rolled samples undergoing again at 435C.

After aging the 435˚C samples, some XRD results came back with an unexpected behavior. In the case of the Aubert Duval cold rolled steel, an inexplicable shift of the peak to a larger angle ($\Delta 2\theta \approx +0.57^{\circ}$) arises after scouring. One possibility is that a diffractometer miscalibration happened before that acquisition; no measurement with the reference sample was performed at that time. Another possibility is that since both apparent drifts took place after a scouring, that this process has removed a thin layer of metal near the surface which revealed a depth under different, greater, residual stress. For the lab rolled sample, a similar problem arises immediately after baking. Three peaks showed on the diffraction pattern, though all three appear shifted, this time, to smaller angles by approximately $\Delta 2\theta \approx -0.8^{\circ}$. Again, this is difficult to explain with any physical change in the metal. In both cases, the samples were scanned again at other times and revealed behavior as-expected; a hardware calibration shift seems possible.

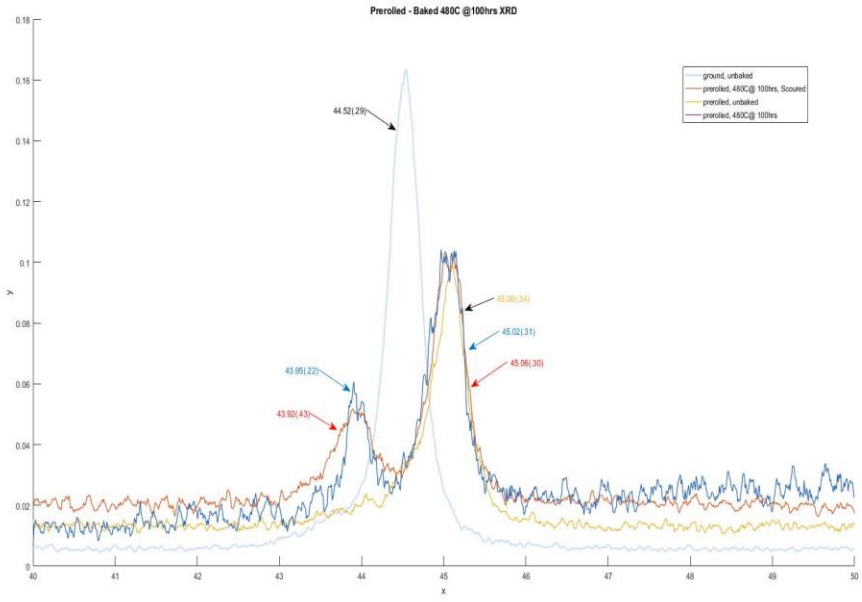

Figure 42. Aubert Duval aging at 480C 100 hours

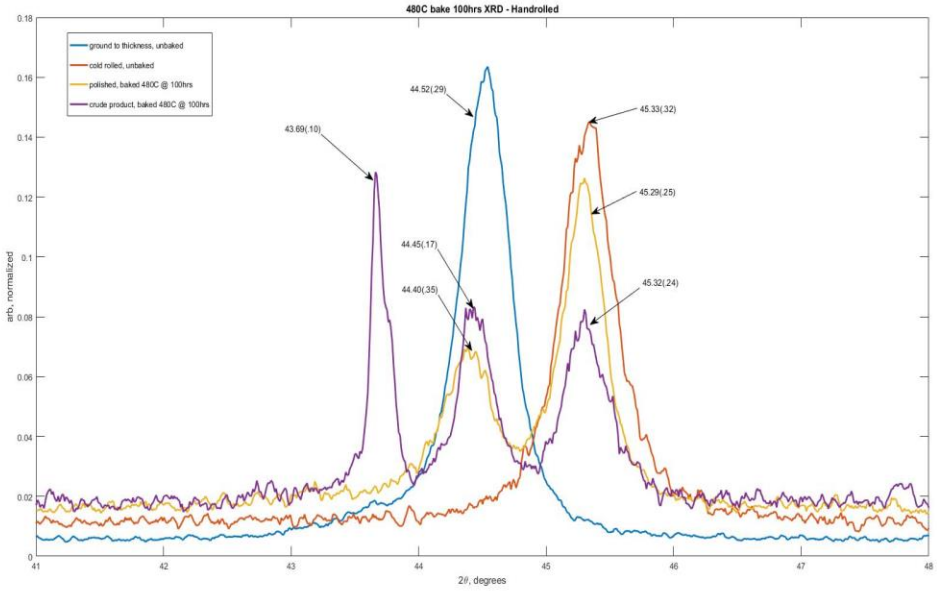

Figure 43. Bake of Lab-Rolled samples at 480˚C for 100 hours

It is also interesting to evaluate the measurements made with baking at 480˚C for 100 hours. There is a 43.69˚ peak that turned out to be an oxide by scouring, though surprisingly doesn't arise for the Aubert Duval cold rolled samples. In the 435˚C run for the lab rolled sample, which appeared to have the results shifted, a similar peak is apparent.

Despite the strange calibration changes and the appearance of oxidation peaks, it seems reasonable to conclude that the α-(110) peak did not shift substantially towards the relaxed value during the precipitation process. The cold-rolling-induced shift in XRD peaks is attributed to residual stress; the fact that it survives the precipitation stage strengthens the supposition that residual stress protects the material from stress corrosion. Table 5 consolidates the results from all precipitate and over-precipitate samples.

Table 5

Relaxation of Residual Stress After Re-Aging

Description	Aging Temp(˚C)	$2\theta(^{\circ})$		$\epsilon_{f\perp}$	Relaxation $\%_{change} = \left(\frac{\epsilon_{f\perp} - \epsilon_{i\perp}}{\epsilon_{i\perp}}\right)$
		Before	*After*		
GM (GTT)	N/A	44.51	44.61	-0.001230	N/A
AD (CR)	435	45.06	44.99	-.009240	-13.6
LR (CR)	435	45.32	45.27	-0.01505	-6.40
AD (CR)	480	45.06	45.06	-0.01070	0.0
LR(CR)	480	45.33	45.29	-0.01545	-5.06

2.4 Problems with Reproduction of the Results for Lab Rolled Samples

Several additional samples were prepared for shipping to research partners for further testing. In the process of gathering and preparing these samples, an anomalous behavior arose from newly produced lab rolled strips. In previous LR strip production, a reduction of 25% thickness led to a shift of $\Delta 2\theta \approx .8°$. In the new strips produced several months later it apparently ceased to produce any shift. Attempts to reproduce the result were unsuccessful, and this is a significant problem. Thus far, 4 additional samples have been prepared using the lab roller; all returned results indistinguishable from ground to thickness samples. The cause of this behavior is still unknown, and casts doubt on the previous results. Parallel tests with Aubert Duval cold rolled samples in this time did not produce any unusual result, and even further shifted when cycled in the crank-roller.

Residual stress is almost certainly present in these samples after the rolling; If two strips are cold rolled in a stack, they will curl away from one another due to differential residual stress [34]. Such a sample also returned ground-to-thickness-like results. Assuming this is true, the question becomes why are we no longer able to measure the normal stress in the lab rolled samples? Are the additional samples made of a different material even if they come from the same pack?

Another possibility is that the previous experiment with lab rolled samples simply acquired incorrect results from XRD. If this is true, then the utility of using XRD to determine residual stress with our setup is put in doubt. This seems unlikely but must be tested regardless by measuring residual stress in a different way. There are multiple way of doing this.

No explanation is yet confirmed.

2.5 Effect of Residual Stress on Electron Energy in Frustrated Bonds

If the VIRGO blades operate with surface tension at 50% of .2% yield stress, then an approximate numerical value for surface stress is readily calculable.

$$\sigma_s = 0.5\sigma_{.2y} = 890\ Mpa$$

By adding the measured residual compressive stress to surface bending stress, this implies a net reduction in magnitude.

$$\sigma_{net} = \sigma_{residual} + \sigma_{bend} < 590 Mpa$$

After this, approximately 66% of original tension remains. Because $E \sim \varepsilon^2$, the free energy from strain is reduced to ≤44% of previous amount, based on the conservative estimations for residual stress. This is a substantial change and can explain increased lifetime of cold rolled blades.

CHAPTER 3

Conclusion

The effectiveness of residual stress inhibiting SCC was suggested, it depends on many factors. It was shown that in the case of cantilever blades, cold rolling is potentially useful because during bending operation, the compressive residual stress left in surface regions by cold rolling overlaps with the area of greatest tension and most susceptible to SCC [41]. The net result is less Mode 1 stress in the surface region where cracks initiate. Because the lowering of the energy barrier to corrosion is quadratic with micro-tension, the protection effect may be substantial.

A possible worry is that the compressive stress on the surface entails a greater tension deeper in the metal, where cracking is still possible; deeper regions are subject to less bending tensional stress and are not exposed to SCC, which starts only at the surface.

3.1 Notes on XRD Findings

The findings outlined in chapter 2 are a positive sign for the theory that residual stress in the cold rolled protects them from stress corrosion. The existence of a surface normal compressive strain is a strong indicator that a biaxial compressive stress is present. This was not directly observed but is a logical inference after the results of this research. The actual compressive residual stress may be substantially greater than 300MPa but no other values can be attained without more information. Some skepticism is necessary for all calculations of residual stress given the experimental methods, as well as the plastic behavior of the metal during cold rolling once the elastic limit is exceeded. The inconsistency in the XRD results is troubling and indicates that either the source of

the inconsistency is identified, or alternative ways to confirm the presence of the residual stress are necessary.

If the estimations were correct, the 300 MPa residual compressive stress calculated from the XRD measurements is approximately 16% of the yield stress. The applied tensional stress on the top surface of a suspension blade is typically 50% of the yield stress; even a reduction of 16%, to 34%, is very substantial and could explain why cold rolled blades survive better than ground-to-thickness ones. Especially so, given the proportionality of electron energy to ϵ^2. It's also entirely possible that the real residual compressional stress is greater than the measured values due to plastic deformation in the surface normal direction exceeding the plasticity limit; this could not be tested with our methods [40].

3.2 Proposed Solutions to the Stress Corrosion Problem

If these results are accepted, or if upcoming experiments confirm that cold-rolling-induced residual compressional stress in the maraging steel blades inhibits SCC, then cold rolling should be used instead of grinding to reduce the blades to their design thickness, or grinding should be limited to the bottom face of a cold rolled strip, without affecting the top. This way, the face under tensional stress will still retain its compressive stress leftover from cold rolling. Of course, this may lead to undesired curling of the blade that must be considered before utilization.

A practical solution is to provide a protective coating or elastic film to keep humidity away from the metal surface. An ultra-high-vacuum compatible solution is to apply a polyimide (Kapton) film that can be painted and then polymerized on the surface.

Simply greasing the blades with UHV grease is a possible solution also worth considering.

3.3 Future work

It is expected that this project will be taken over by Matthew Gonzales at CSULA, to confirm that the residual stress in cold rolled maraging steel blades is the factor that allows them to better survive an exposure to ambient humidity.

The first step will be to finalize the preparation of the strips which will be sent to Prof. Lorenzo Valentini in Pisa for additional tests. Right now, Aubert Duval cold rolled, and ground-to-thickness strips are ready, but the mysterious issues regarding missing XRD shifts in lab rolled samples must be solved.

Table 6

Strips to prepare for sending to partners in Pisa, Italy.

Sample Specification	**Quantity**
GTT Strips	2
Aubert Duval (CR) Strips	2
Lab-Rolled Strips	2
GTT Strips, *Aged*	2
Aubert Duval (CR) Strips, *Aged*	2
Lab-Rolled Strips, *Aged*	2

3.3.1 Depth Stress Profiling

Perhaps the most important and conclusive test to come, is the stress profiling of cold rolled steel samples. While XRD is a useful way to study stress and strain at the metal surfaces, it does not describe behavior more than a few microns into the metal which is relevant for SCC.

There are several ways to do this, but right now the expectation is to use the center-hole drilling method. Surface layer removal by chemical means is another way of revealing new depths of the metal to XRD as a way of measuring residual stress.

3.3.2 Hydrogen Measurements

A technique is available to determine the presence of hydrogen trapped within the iron lattice, both in bulk and near cracks. Because hydrogen represents such a common path to failure in high strength steels, it was supposed that it provided a mechanism for corrosion failure. Hydrogen is injected in the metal in humidity driven oxidation, the little hydrogen found in the failed samples by other researchers may be an effect, not a cause of stress corrosion.

3.3.3 Controlled Humidity Tests

The conclusive test would be to produce many blades of both kinds, subject them to bending stress under changing humidity conditions and monitor the failure frequency. This is clearly a large-scale endeavor, well beyond what possible with presently available resources.

REFERENCES

1. Accadia, T., Acernese, F., Antonucci, F., Astone, P., Ballardin, G., Barone, F., et al. (2011). The seismic superattenuators of the virgo gravitational waves interferometer. *Journal of Low Frequency Noise, Vibration and Active Control, 30*(1), 63-79. doi:10.1260/0263-0923.30.1.63
2. Van Heijningen, J. V. (2016). *Hydrogen migration in GAS blades due to hydrostatic stress gradients*. LSC-Virgo Collaboration Meeting
3. Totten, G. (2002). In Totten G. E., Howes M. A. H. and Inoue T. (Eds.), *Handbook of residual stress and deformation of steel*. Materials Park, OH; Materials Park, Ohio: Materials Park, OH : ASM International.
4. Abbott, Abernathy, et al. (2016). GW151226: Observation of Gravitational Waves from a 22-Solar-Mass Binary Black Hole Coalescence. *Physical Review Letters, 116*(24), 241103.
5. Einstein, A (1918). "Über Gravitationswellen". *Sitzungsberichte der Königlich Preussischen Akademie der Wissenschaften Berlin*. part 1: 154–167
6. Calloni, E. (2017). Introduction to gravitational wave detection and advanced virgo status and perspectives. *Nuclear and Particle Physics Proceedings, 291-293*, 127-133. doi:10.1016/j.nuclphysbps.2017.06.026
7. Leslie, W. (1981). The physical metallurgy of steels (McGraw-Hill series in materials science and engineering). Washington : New York: Hempisphere Pub. ; McGraw-Hill.
8. Trebuňa, F. , Bocko, J. , Šimčák, F. , & Buršák, M. (2013). Analysis of Failures of Leaf Springs on the Continuous Casting Machines. *American Journal of Mechanical Engineering*, *1*(7), 304-308
9. Habiby, F., Siddiqui, T., Hussain, N., Ul Haq, H., & Khan, A. (1996). Lattice changes in the martensitic phase due to ageing in 18 wt% nickel maraging steel grade 350. Journal of Materials Science, 31(2), 305-309.
10. Aubert & Duval. (2017). *Steel MARVAL18 X2NiCoMo18-8-5*. Unpublished manuscript.
11. Service Steel Aerospace Corp. (2018). *Maraging Data Sheet*
12. O. Moshka, M. Pinkas, E. Brosh, V. Ezersky, L. Meshi, Addressing the issue of precipitates in maraging steels – Unambiguous answer, Materials Science and Engineering: A, Volume 638, 2015, Pages 232-239, ISSN 0921-5093, https://doi.org/10.1016/j.msea.2015.04.067.
13. Casati, R., Lemke, J., Tuissi, A., & Vedani, M. (2016). Aging Behaviour and Mechanical Performance of 18-Ni 300 Steel Processed by Selective Laser Melting. *Metals, 6*(9), 218.
14. Farooque, M., Ayub, H., Ul Haq, A., & Khan, A. (1998). The formation of reverted austenite in 18% Ni 350 grade maraging steel. Journal of Materials Science, 33(11), 2927-2930.
15. Moverare, J., (2005). Shrinkage and ageing of Ni-base alloys at intermediate temperatures (400-600°C). Finspång: Siemens Industrial Turbomachinery AB. Internal technical report 1CS51497.
16. Trethewey, K., & Chamberlain, J. (1995). Corrosion for science and engineering (2nd ed.). Harlow, England: Longman.

17. Jones, R. (1992). Stress-corrosion cracking. Materials Park, Ohio: ASM International.
18. Shreir, L. L. (Ed.). (2013). *Corrosion: Metal/Environment reactions* (2nd ed.). Newnes: Elsevier Science.
19. Boresi, A. P, Schmidt, R. J. and Sidebottom, O. M., 1993, *Advanced Mechanics of Materials*, Wiley.
20. Jaeger, J. C. Elasticity, Fracture and Flow. London: Chapman & Hall, 1969.
21. E P Popov; Sammurthy Nagarajan; Z A Lu. "Mechanics of Material". Englewood Cliffs, N.J. : Prentice-Hall, ©1976, p. 119, "Pure Bending of Beams", ISBN 978-0-13-571356-3
22. Christopher, T., Sankarnarayanasamy, K., & Rao, B. (2004). Fracture behaviour of maraging steel tensile specimens and pressurized cylindrical vessels. *Fatigue & Fracture of Engineering Materials & Structures, 27*(3), 177-186.
23. Fett, T. (2002). Stress intensity factors and T-stress for single and double-edge-cracked circular disks under mixed boundary conditions. *Engineering Fracture Mechanics, 69*, 69-83.
24. ASM International, *Metals Handbook (Desk Edition)* Chapter 32 (Failure Analysis), American Society for Metals
25. Reliance Foundry Co. (2017). *Hot rolled vs. cold rolled steel.* Retrieved 05/01, 2018, from Jul 26, 2017
26. Gurinder Singh Brar. (2017). Finite Element Simulation of Residual stress Formation in cold Rolling Process. Research Journal of Engineering and Technology, Research Journal of Engineering and Technology, Dec 30, 2017.
27. De Giorgi, M. (2011). Residual stress evolution in cold-rolled steels. *International Journal of Fatigue, 33*(3), 507-512.
28. Determination of Residua Stresses by X-Ray Diffraction – Issue 2 Fitzpatrick
29. Lu, Yu, & Sisson. (2017). The effect of carbon content on the c/a ratio of as-quenched martensite in Fe-C alloys. Materials Science & Engineering A, 700, 592-597.
30. Hildebrand, H. (1997). The yield strength of iron alloys and the contribution of lattice bond. Materials Science & Engineering A, 234, 145-148.
31. HUNG, Nguyen Van; HUE, Trinh Thi; DUC, Nguyen Ba. Calculation of Morse Potential Parameters of bcc Crystals and Application to Anharmonic Interatomic Effective Potential, Local Force Constant. VNU Journal of Science: Mathematics - Physics, [S.l.], v. 31, n. 3, sep. 2015. ISSN 2588-1124
32. Miller indices. (2018). *Britannica Online Academic Edition,* Encyclopædia Britannica, Inc
33. M.E. Fitzpatrick, A.T. Fry, P. Holdway, F.A. Kandil, J. Shackleton and L. Suominen. (2005). *Measurement good practice guide no. 52 determination of residual stresses by X-ray diffraction – issue 2* (Good Practice Guide No. 2). Teddington, Middlesex, United Kingdom: National Physical Laboratory.
34. Murray, C., Bedell, & Ryan. (2013). Weighted mechanical models for residual stress determination using x-ray diffraction. *Journal of Applied Physics, 114*(3), Journal of Applied Physics, 21 July 2013, Vol.114(3).
35. Schajer, G. (2013). Practical residual stress measurement methods.

36. Eric A. Jägle, Zhendong Sheng, Philipp Kürnsteiner, Sörn Ocylok, Andreas Weisheit, & Dierk Raabe. (2016). Comparison of Maraging Steel Micro- and Nanostructure Produced Conventionally and by Laser Additive Manufacturing. *Materials, 10*(1), 8.
37. Lester, H. H., and Aborn, R. H. Behavior Under Stress of the Iron Crystals, Army Ordnance, v. 6, 1925, 1926, pp. 120, 200, 283, 364
38. Industrial Engineering; Studies from A. Lim and Co-Researchers in the Area of Industrial Engineering Reported (Effect of Deep Cold Rolling on Residual Stress Distributions Between the Treated and Untreated Regions on Ti-6Al-4V Alloy). (2016, November 14). *Journal of Engineering*, p. 1594.
39. Lian, Yong, Huang, Jinfeng, Zhang, Jin, Zhao, Chao, Gao, Wen, Zhang, Zunjun, & Ma, Minyu. (2018). Effects of cold rolling on the microstructure and properties of Fe-Cr-Ni-Mo-Ti maraging steel. *Materials Science & Engineering A, 712*, 663-670.
40. Giancarlo Pepponi, Saulius Gražulis, and Daniel Chateigner: MPOD: a Material Property Open Database linked to structural information. Nuclear Instruments and Methods in Physics Research B 284, 2012, 10-14
41. Matsuda, M., Ootsuki, E., Kajihara, S., Hanawa, Y., & Hamada, T. (2011). *Predicting effect of cold rolling on fatigue strength under combined loading.* Unpublished manuscript.